frontiers | Frontiers in Marine Science

Check for updates

# Seasonal variability of upper ocean primary production along the Kuroshio off Japan: Roles of eddy-driven nutrient transport

Xu Zhang[1], Yusuke Uchiyama[2]*, Eiji Masunaga[3], Yota Suzue[4] and Hidekatsu Yamazaki[5,6,7]

[1]Laboratory for Climate and Ocean-Atmosphere Studies, Department of Atmospheric and Oceanic Sciences, School of Physics, Peking University, Beijing, China, [2]Department of Civil Engineering, Kobe University, Kobe, Japan, [3]Global and Local Environmental Co-creation Institute, Ibaraki University, Hitachi, Japan, [4]Construction Technique Institute Engineering Co., Ltd., Nagoya, Japan, [5]Department of Ocean Sciences, Tokyo University of Marine Science and Technology, Tokyo, Japan, [6]Alpha Hydraulic Engineering Consultants Co., Ltd., Tokyo, Japan, [7]College of Marine Ecology and Environment, Shanghai Ocean University, Shanghai, China

We assessed spatial and seasonal variabilities of eddy-driven vertical nutrient fluxes, which are essential for maintaining primary production in the upper ocean. A climatological model based on a Regional Oceanic Modeling System (Regional Oceanic Modeling System) coupled with a Nutrient Phytoplankton Zooplankton and Detritus (NPZD) biogeochemical model at a submesoscale eddy-permitting resolution was used to investigate the mechanisms driving such variabilities around the Kuroshio, off the coast of Japan. The model realistically reproduced the spatial segmentations in primary production on both sides of the Kuroshio path with a higher chlorophyll-a concentration on the northern side than the southern side. In winter, downward eddy-induced nitrate flux is predominantly provoked in the upstream Kuroshio region (KR), while upward nitrate fluxes prevail in the downstream Kuroshio Extension (KE) region, due to both shear and baroclinic instabilities. Baroclinic instability plays a crucial role in inducing seasonal variability, leading to enhancement (reduction) of the eddy flux in winter (summer), particularly in regions away from the Kuroshio axis. Furthermore, we found that the influence of the Izu-Ogasawara Ridge, located in the KR, on regional dynamics and resultant spatial variability of the biogeochemical response are mostly confined in the KR. The Kuroshio is less turbulent in the upstream of the ridge, while it becomes unstable to shed mesoscale eddies in laterally wider and vertically deeper regions downstream. Consequently, although the near-surface nitrate concentration is lower downstream, the upward eddy-driven nitrate flux is more effective in maintaining active primary production due to the shear and baroclinic instabilities in winter.

# 1 Introduction

Carbon exchange between the atmosphere and ocean substantially regulates climate change. Previous studies have reported that approximately one-half of total $CO_2$ emissions are taken up by a combination of terrestrial and marine carbon reservoirs (e.g., Schimel et al., 2001; Ballantyne et al., 2012). Nellemann et al. (2009) reported that 55% of all biological carbon is captured by marine organisms, commonly referred to as "blue carbon". Falkowski et al. (1998) showed the biogeochemical controls and feedbacks on global ocean primary productivity, which are responsible for pelagic blue carbon. Meanwhile, carbon cycling in coastal waters is a major component of global carbon cycles and budgets (Bauer et al., 2013). In general, localized upwelling due to mesoscale cyclonic eddies brings nutrient-rich subsurface water to the surface to enhance near-surface primary productivity. Particularly in pelagic upper ocean, subsurface nutrients are the only source, which are greatly influenced by vertical transport due to eddy-induced localized upwelling (e.g., Falkowski et al., 1991). Satellite observations revealed that spatial variability in surface chlorophyll was distributed on both mesoscale and submesoscale. Numerical simulations have also been conducted with particular concerns about biological responses to mesoscale and submesoscale variability. It has been recognized that biogeochemical cycles could be affected by mesoscale eddies in the global upper ocean (e.g., Chelton et al., 2011; Gaube et al., 2013). For instance, Lee and Kim (2018) investigated regional variability and turbulent characteristics of submesoscale surface chlorophyll concentrations and demonstrated that spring (fall) blooms are more active in the coastal areas in the Japan sea because of the stronger submesoscale horizontal shear and vertical processes that increase vertical mixing. Liu and Levine (2015) also concluded that the chlorophyll concentration was increased by 38% on average (83% maximum) at submesoscales during the cold season in the North Pacific Subtropical Gyre. The offshore transport of nutrients and carbon driven by filaments and mesoscale eddies in the California Current System was discussed based on a coupled physical-biogeochemical model in a climatological configuration (Nagai et al., 2015).

The Kuroshio is one of the most energetic western boundary currents accompanied by vigorous eddy activity at mesoscale and submesoscale. It originates from the eastern area of Philippines, drifts north along the East China Sea shelf, and veers northeast to flow past the southern coast of Japan. The Kuroshio then separates from the shelf near 140°E and 35°N, forming a free jet known as the Kuroshio Extension, in the North Pacific Ocean (Kawai, 1972; Qiu, 2002). Both nutrient concentrations and their inventories in the northern South China Sea are affected by abrupt Kuroshio intrusions through the Luzon Strait on seasonal scales (Du et al., 2013). The total annual nitrogen input due to the frontal eddies could result in a carbon production rate of 40 g C m$^{-2}$ y$^{-1}$ in the Enshunada Sea (Kimura et al., 1997; Nakata et al., 2000). Kaneko et al. (2013) reported that segmentation of vertical nitrate fluxes on both sides of the Kuroshio is observed in the Kuroshio region (hereinafter referred to as KR; see the thick black box in Figure 1A). Kodama et al. (2014) analyzed seasonal and spatial variabilities of nitrate concentration in the upper ocean along 138°E in the KR and demonstrated a higher value in winter. In the eastern part of the KR, the Kuroshio passes over the Izu-Ogasawara Ridge, a unique shallow topography consisting of two major island chains located off the south coast of Japan along 140–141°E. Sugimoto and Hanawa (2012) reported that the Kuroshio tends to be unstable downstream after it passes over the shallower part of the ridge at a depth of ~1000 m, leading to intense eddy mixing. Studies on the volume transport of the Kuroshio (e.g., Isobe and Imawaki, 2002) and the westward propagation of eddies near the Izu-Ogasawara ridge (e.g., Ebuchi and Hanawa, 2001; Xu et al., 2016) have been extensively conducted despite the lack of biogeochemical connections. In contrast, in the Kuroshio Extension (KE) region (east of M5 in Figure 1B), primary production in spring is occasionally lowered by a lack of nitrate and silicic acid (Nishibe et al., 2015). Intermittent nutrient transport induced by ageostrophic vertical circulation and mixing has been detected on a timescale of a few days near the Kuroshio front in the KE (Clayton et al., 2014) due to the combination of diabatic turbulence and adiabatic subduction (Nagai et al., 2012). The importance of cyclonic (anticyclonic) eddy generation and related eddy core migration for enhancement (reduction) of phytoplankton production in the KE has been discussed (e.g., Sasai et al., 2010; Kouketsu et al., 2014). More recently, a climatological model (Uchiyama et al., 2017) showed significant differences of the biogeochemical responses to eddy activities in the KR and KE. In the KR, persisting cyclonic eddies developed between the Kuroshio and coastline are responsible for upwelling-induced eutrophication. However, the eddy-induced vertical nutrient flux counteracts and promotes pronounced southward and downward diapycnal nutrient transport from the mixed-layer down beneath the main body of the Kuroshio, which suppresses the near-surface productivity. In contrast, the KE has a 23.5% higher productivity than the KR, even at comparable eddy intensity. Upward nutrient transport prevails near the surface due to predominant cyclonic eddies, particularly to the north of the KE, where the downward transport barely occurs, except at depths deeper than 400 m and to a much smaller degree than in the KR. In addition to abundant mesoscale eddies shed around the Kuroshio, smaller but more intensive submesoscale eddies with sizes of $O$ (1-10 km) are known to appear mainly in colder seasons due to the mixed-layer deepening and surface cooling (e.g., Kamidaira et al., 2018). Although submesoscale eddies are mostly confined in the surface mixed layer, they promote quite energetic vertical secondary circulations that are anticipated to
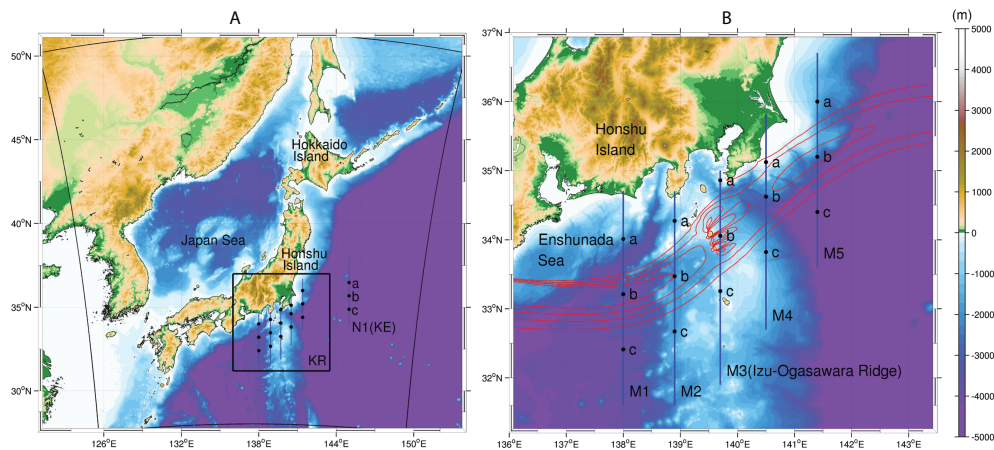
**FIGURE 1**
**(A)** The ROMS-NPZD model domain encompassing the Kuroshio Region (KR) and the Kuroshio Extension Region (KE). The thick black box indicates the KR, while the outer square corresponds to the perimeter of the model domain. The blue line annotated with N1 is the selected transect along 145°E, a representative of the KE, with three black dots on N1 showing the sampling locations for Hovmöller plots (Figure 4). **(B)** The enlarged view of **(A)** corresponding to the black box in **(A)**. The five blue lines represent the selected transects along 138°E, 138.9°E, 139.7°E, 140.5°E, and 141.4°E in the KR, named M1-M5, that are used for the subsequent analyses. The black dots on M1-M5 again show the locations used for Hovmöller plots in Figures 3, 6–8. Red contours indicate the approximate Kuroshio path with surface velocity magnitudes ≥ 0.5 m/s at intervals of 0.3 m/s. Colors are bathymetry.

enhance vertical transport of subsurface nutrient and thus to affect upper-ocean primary production.

There are abundant studies concerning seasonal and interannual variabilities of primary production and related parameterization, including those conducted by Uitz et al. (2010), who analyzed seasonal and interannual variabilities of global phytoplankton class-specific primary production. Analyses in several specific regions have also been undertaken. For example, subsurface chlorophyll maxima (SCM) are seasonal features and have strong effects on depth-integrated primary production estimates in the Arctic Ocean when the surface nitrate is depleted, while its interannual variability is very limited (Ardyna et al., 2013). For SCM, Cullen (2015) summarized that phytoplankton growth is controlled by a balance between available light intensity and nutricline depth, presumably influenced by seasonal variations in vertical nitrate flux that could directly change the structure of SCM. Lomas et al. (2012) reported seasonal primary production on the Eastern Bering Sea shelf in spring and summer 2008 and 2009, concluding that the integrated rate of net primary production is generally lower in summer, while phytoplankton growth rate is higher. The pattern of seasonally integrated primary production dynamics in the Kara Sea, Russia, was discussed based on satellite data obtained in 2003–2015 (Demidov et al., 2017). Seasonal variability of the integrated net primary production dominates over the interannual signal in the Mediterranean Sea (Lazzari et al., 2012). However, studies on the seasonal variability of the primary production in the KR and

KE are limited, particularly in conjunction with the eddying Kuroshio currents affected by the ridge topography in the KR.

In the present study, we aimed to analyze the seasonal variability of eddy-driven vertical nutrient fluxes that play essential roles in maintaining upper-ocean primary production, as well as its driving mechanisms in the KR and KE regions. To this end, we employed a high-resolution model based on the Regional Oceanic Modeling System (ROMS; Shchepetkin and McWilliams, 2005; Shchepetkin and McWilliams, 2008) coupled with a nitrogen-based nutrient, phytoplankton, zooplankton, and detritus (NPZD) biogeochemical model described by (Fasham et al., 1990). The model is initialized by the assimilative Japan Coastal Ocean Predictability Experiments (JCOPE2) oceanic reanalysis (Miyazawa et al., 2009) and is run in a climatological configuration for 10 years. This model was originally developed and validated in a previous study (Uchiyama et al., 2017), where the annually averaged eddy-driven nitrate fluxes were discussed to highlight the opposing downward and upward vertical nutrient supply in the KR and KE regions, emphasizing that downward nutrient flux suppresses primary production in the KR. In contrast, the present study was focused on the seasonal variability of eddies and associated vertical nutrient fluxes along the Kuroshio path (or axis) around the KR and KE regions with additional emphasis on the ridge topography. The remainder of this paper is organized as follows. The design and configuration of the coupled model are described in Section 2. Section 3 introduces the model results including the seasonal

variability of surface biogeochemistry and eddy activity in relation to the Kuroshio dynamics, as well as the effects of the oceanic ridge in the KR. The dynamics and the eddy generation mechanisms are discussed in Section 4, followed by concluding summary in Section 5.

## 2 Methods

### 2.1 Ocean circulation model

We exploited a downscaling ocean circulation model based on the Regional Oceanic Modeling System (ROMS; Shchepetkin and McWilliams, 2005; Shchepetkin and McWilliams, 2008), coupled with a nitrogen-based pelagic NPZD biogeochemical model (Section 2.2), encompassing both KR and KE regions (Uchiyama et al., 2017). The initial and side boundary conditions for the ROMS were provided by monthly climatology of the assimilative JCOPE2 oceanic reanalysis (Miyazawa et al., 2009). A one-way offline nesting technique was employed to convey the parent JCOPE2 to the child ROMS model with grid resolution refinement (e.g., Mason et al., 2010; Uchiyama et al., 2014; Kamidaira et al., 2017; Uchiyama et al., 2017; Kamidaira et al., 2018; Uchiyama et al., 2018a; Uchiyama et al., 2018b; Uchiyama et al., 2018c; Tada et al., 2018; Masunaga et al., 2018; Kamidaira et al., 2019; Masunaga et al., 2019; Zhang et al., 2019; Kurosawa et al., 2020; Kamidaira et al., 2021; Takeda et al., 2021; Uchiyama et al., 2022; Masunaga et al., 2022; Matsushita et al., 2022). Therefore, the horizontal grid spacing was successfully reduced from 1/12° (~10 km) of the JCOPE2 reanalysis to 3 km of the ROMS model, and vertically into stretched 32 s-layers (Shchepetkin and McWilliams, 2005) with grid height refinement near the surface and bottom to adequately resolve the boundary layers. We employed the K-Profile Parameterization (KPP) mixed-layer turbulence model described in Large et al. (1994) and Lemarié et al. (2012) to represent the vertical momentum and tracer mixing. With a 3-km grid resolution, the present model is considered to be a submesoscale eddy-permitting model, in which submesoscale eddies are marginally represented (e.g., Uchiyama et al., 2017). The SRTM30_PLUS product (Rodriguez et al., 2005; Rodriguez et al., 2006; Becker et al., 2009) at a 30 arc second resolution complemented by the J-EGG500 (http://www.jodc.go.jp/data_set/jodc/jegg_intro.html) data set at a 500 m resolution was utilized to represent the bathymetry. The ROMS model was forced by the daily climatology of the GPV-GSM surface wind stress (Roads, 2004) provided by the Japan Meteorological Agency (JMA). The surface heat and freshwater fluxes were obtained from the monthly climatology of the Comprehensive Ocean-Atmosphere Data Set (COADS; Woodruff et al., 1987). Additionally, four-dimensional temperature and salinity (TS) nudging (also known as robust diagnostic; e.g., Marchesiello

et al., 2003) was used to improve the Kuroshio path reproducibility, with a weak nudging inverse time scale of 1/20 per day. Table 1 summarizes the detailed numerical configurations of the ROMS models.

### 2.2 Biogeochemical model

We employed a simple nitrogen-based pelagic NPZD biogeochemical model based on (Fasham et al. 1990), with a modification described by Gruber et al. (2006), where we consider five components: nitrate$[NO_3^-]$, ammonium $[NH_4^+]$, phytoplankton [Phyt], zooplankton [Zoo] and detritus [Det]. The conservation equations are given as follows:

$$\frac{D}{Dt}[NO_3^-] = -Q_1, \tag{1}$$

$$\frac{D}{Dt}[NH_4^+] = -Q_2 + \mu_{[Zoo][NH_4^+]} \cdot [Zoo] + \mu_{[Det][NH_4^+]} \cdot [Det], \tag{2}$$

$$\frac{D}{Dt}[Phyt] = -\left(\mu_{[Phyt]} + \mu_{[Phyt][Det]}\right) \cdot [Phyt] - G + Q_1 + Q_2, \tag{3}$$

$$\frac{D}{Dt}[Zoo] = -\left(\mu_{[Zoo]} + \mu_{[Zoo][NH_4^+]} + \mu_{[Zoo][Det]}\right) \cdot [Zoo] + \beta \cdot G, \tag{4}$$

$$\frac{D}{Dt}[Det] = -\left(\mu_{[Det]} + \mu_{[Det][NH_4^+]}\right) \cdot [Det] + (1 - \beta) \cdot G$$
$$+ \mu_{[Phyt][Det]} \cdot [Phyt] + \mu_{[zoo][Det]} \cdot [Zoo], \tag{5}$$

where $D/Dt$ is the material derivative that includes 3-D advection, vertical settling of [Phyt], [Zoo] and [Det], and vertical eddy diffusive fluxes computed by the KPP model (Large et al., 1994). $Q_1$ indicates the rate of nitrate uptake by phytoplankton, $Q_2$ denotes the rate of ammonium uptake

TABLE 1   Ocean circulation model configurations.

| Model configurations | Data used |
|---|---|
| Computational period | Climatological 10 years |
| Grid cells | 784 × 864 (× 32 layers) |
| Horizontal grid resolution | 3 km |
| Baroclinic time step | 150 s |
| Surface wind stress | JMA-GSM (daily climatology) |
| Surface flux | COADS (monthly climatology) |
| Boundary/Initial condition | JCOPE2 (monthly climatology) |
| T-S nudging | JCOPE2 (10-day averaged climatology) |
| Topography | SRTM30+JEGG500 |

STRM30: SRTM30_PLUS (Rodriguez et al., 2005; Rodriguez et al., 2006; Becker et al., 2009).
J-EGG500 (http://www.jodc.go.jp/data_set/jodc/jegg_intro.html).

by phytoplankton, and $G$ is the rate of phytoplankton grazing by zooplankton. These three terms are given by:

$$Q_1 = \frac{\alpha_J \cdot [Phyt] \cdot [NO_3^-] \cdot e^{-\varnothing \cdot [NH_4^+]}}{K_{NO_3^-} + [NO_3^-]}, \quad (6)$$

$$Q_2 = \frac{\alpha_J \cdot [Phyt] \cdot [NH_4^+]}{K_{NH_4^+} + [NH_4^+]}, \quad (7)$$

$$G = \frac{g_{max} \cdot [Phyt] \cdot [Zoo]}{K_{Phyt} + [Phyt]}. \quad (8)$$

where $\alpha_j$ is the light limited growth rate, with unit of d$^{-1}$, as a function of photosynthetically active radiation (PAR) and maximum growth rate (see Eqs. 4-5 in Fasham et al., 1990). The other model parameters are summarized in Table 2.

The seasonal climatology of the World Ocean Atlas 2005 (WOA05. e.g., Garcia et al., 2006) and the monthly climatology of the MODIS/Aqua satellite data (https://oceandata.sci.gsfc.nasa.gov/MODIS-Aqua/) provided the initial and lateral boundary conditions for nitrate and phytoplankton. In the present study, we followed the configuration described by Gruber et al. (2006) and Uchiyama et al. (2017) to set zooplankton to be proportional to chlorophyll-$a$ (Chl-$a$) concentration for its initial and boundary conditions. Meanwhile, ammonium and detritus were initialized to zero. More details on the modeling approach of the current ROMS-NPZD model are reported in Uchiyama et al. (2017). The model was run for 10 years in a climatological mode, and the results for the last (10$^{th}$) year of data were used for the following analyses.

The present study investigates the upper-ocean primary production, which is synthesis of organic compounds from $CO_2$, mainly by photosynthesis that uses light as its energy while it often appears through chemosynthesis that relies on oxidation as the energy. Yet photosynthesis and primary production are not the same concept, Chl-$a$ concentration and primary production are closely related to each other. For example, Behrenfeld et al. (1998) evaluated the primary production from Chl-$a$ concentration with an empirical relation:

$$\log_{10} P = 0.559 \log_{10} C + 2.793, \quad (9)$$

where $P$ is primary production with the unit of mgC m$^{-2}$ d$^{-1}$, $C$ is the Chl-$a$ concentration with the unit of mgC m$^{-3}$. Because $P$ could be evaluated more complicatedly with Chl-$a$ specific absorption coefficient of phytoplankton, PAR, etc, Eq. (9) is just a simplified representation. Although $P$ may also be evaluated from the nitrate and ammonium uptakes, $viz.$, Eqs (6) and (7), with some assumptions such as the canonical Redfield C/N ratio of 6.625 (e.g., Koné et al., 2005), $in$-$situ$ $P$ is still underway to be quantified precisely and universally (e.g., Oschlies, 2001). Instead, we simply view Chl-$a$ as a good proxy of $P$ relying empirically on Eq. (9) in the present analysis by presuming that spatiotemporal variabilities of $P$ could be qualitatively represented by surface Chl-$a$ field in the study area. Hence, we leave the detailed quantification of $P$ to future works.

# 3 Results

## 3.1 Surface Chl-$a$ and eddy activity

The reproducibility of the hydrodynamic kernel of the present coupled ROMS-NPZD model has been extensively confirmed to show a good agreement in the annual and seasonally averaged values against satellite altimetry and sea surface temperature (SST) data, $in$ $situ$ cross-sectional density measurements, resultant 3D velocity fields, including the

TABLE 2 Biogeochemical model configurations.

| Parameter | Symbol | Value | Unit |
|---|---|---|---|
| Half-saturation for phytoplankton $NO_3^-$ uptake | $K_{NO_3^-}$ | 1.5 | mmol N m$^{-3}$ |
| Half-saturation for phytoplankton $NH_4^+$ uptake | $K_{NH_4^+}$ | 0.5 | mmol N m$^{-3}$ |
| Phytoplankton ammonium inhibition parameter | $\varnothing$ | 1.5 | (mmol N)$^{-1}$ |
| Phytoplankton loss to sink rate | $\mu[Phyt]$ | 0.01 | d$^{-1}$ |
| Phytoplankton mortality to detritus rate | $\mu[Phy][Det]$ | 0.072 | d$^{-1}$ |
| Zooplankton maximum growth rate | $g_{max}$ | 0.75 | d$^{-1}$ |
| Zooplankton assimilation efficiency | $\beta$ | 0.75 | n.d. |
| Zooplankton half-saturation for ingestion | $K_{Phyt}$ | 1.0 | d$^{-1}$ |
| Zooplankton loss to sink | $\mu[Zoo]$ | 0.025 | d$^{-1}$ |
| Zooplankton specific excretion rate | $\mu[Zoo] NH_4^+]$ | 0.1 | d$^{-1}$ |
| Zooplankton mortality to detritus | $\mu[Zoo][Det]$ | 0.025 | d$^{-1}$ |
| Detrital loss to sink rate | $\mu[Det]$ | 0.02 | d$^{-1}$ |
| Detrital breakdown to $NH_4^+$ rate | $\mu[Det][ NH_4^+]$ | 0.03 | d$^{-1}$ |

Kuroshio, and eddy intensity (Uchiyama et al., 2018b). More importantly, the NPZD model was also validated with the climatological satellite Chl-*a* data to show overall agreement, such as enhanced upper-ocean primary productivity enriched by the nutrient stream accompanied by the Kuroshio (Uchiyama et al., 2017; Nagai et al., 2019). Although this simplified nitrogen-based pelagic model is not perfectly correct, Uchiyama et al. (2017) concluded that the present model performs reasonably well in diagnosing biological responses to eddy activities in the upper ocean around the Kuroshio. However, there are several subtle discrepancies between the model and observations, which are generally considered to play minor roles in the present study. For example, modeled primary production is slightly overestimated in the north of the Kuroshio path in the KE compared to satellite observations, likely due to the use of a suboptimal set of the biological parameters and the biogeochemical model equations. Another possible cause may be the lack of an iron limitation mechanism (e.g., Fiechter et al., 2009; Moore et al., 2013). In addition, the Chl-*a* concentration near coastal areas is underestimated because the model ignores land-derived nutrient input that should affect coastal productivity significantly. In turn, as the coastal Chl-a from the satellite is often contaminated by influences of suspended particulate matters (e.g., sediments), the present inconsistency must be diagnosed carefully in future works. It is worth noting that we intentionally excluded the land-derived nutrient source because the primary aim of the present

study was to understand the influence of oceanic eddy dynamics on vertical nutrient transport and their role in sustaining upper-ocean productivity, while avoiding terrestrial influences in the upper ocean that may introduce additional seasonality.

Figure 2 shows the spatial distributions of seasonally averaged surface Chl-*a* concentrations from winter (Dec.–Feb.) to fall (Sep.–Nov.). An obvious spring bloom (Mar.–May) occurs extensively on the northern side of the Kuroshio, between Hokkaido Island (~144°E, 45°N) and the central Honshu Island (~140°E, 35°N), because of abundant nutrient supply from deeper layers to the surface in early spring (Figure 2B). By contrast, although the Chl-*a* concentration on the southern side of the Kuroshio is enhanced slightly, it remains lower than that on the northern side. A possible reason is that the nitrate-depleted subsurface mode water is dominant underneath the south of the Kuroshio (e.g., Nishikawa et al., 2013). The surface Chl-*a* concentration is the lowest in summer (Jun.–Aug.; Figure 2C), and then it generally increases in colder seasons from fall to winter (Figures 2D,A). Meanwhile, the Chl-*a* concentration is the highest in the Japan Sea in winter, compared to other seasons (Figure 2A), which is inconsistent with observations (e.g., Yoo and Kim, 2003; Yamada et al., 2004; Park et al., 2014), most likely due to the lack of the land-derived nutrient input in the model. Nevertheless, the modeled seasonal variability of surface productivity on the Pacific side is largely consistent with the MODIS/Aqua satellite data and previous measurements (Sasai et al., 2007; Nagai et al., 2019). Qualitative
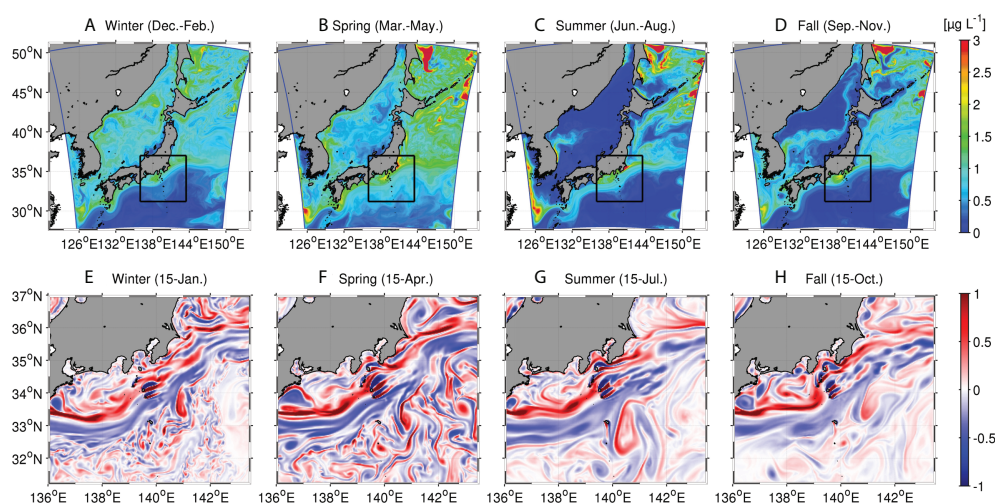


**FIGURE 2**

Upper panels: Seasonally averaged modeled surface chlorophyll-*a* (Chl-*a*) concentrations in four seasons. Note that we define four seasons as winter (December-February), spring (March-May), summer (June-August), and fall (September-November), respectively. Lower panels: Daily snapshots of relative vorticity normalized by the Coriolis parameter at the surface on the middle day of the four seasons. Note that we use the Chl-*a* unit of µg/L here for comparisons to *in-situ* Chl-*a* data (e.g., Hsu et al., 2020). In contrast, phytoplankton concentrations shown in Figures 3, 4 and 7 are depicted with the nitrogen unit of mmol N m$^{-3}$ for comparisons to other nitrogen compartments such as phytoplankton and nitrate to diagnose the nitrogen budget represented by the NPZD model. Nevertheless, the phytoplankton concentration can readily be converted into the Chl-*a* unit with a Chl-*a*:N ratio of 2.0 (see Gruber et al., 2006).

evidence of the importance of eddies to seasonal productivity is demonstrated in the lower panels of Figure 2, in which snapshots of relative vorticity normalized by the local Coriolis parameter at the surface are depicted for the four seasons in the enlarged area (shown in the rectangular black boxes in the upper panels) around the KR and KE regions. While intensive mesoscale vortices are particularly significant around the Kuroshio, submesoscale eddies are generated more evidently in colder seasons, with relatively smaller spatial scales in the northern area (Figures 2E,F). In contrast, mesoscale eddies are more predominant in warm seasons (Figures 2G,H). This area is known to be occupied by intensive submesoscale coherent structures in winter, mainly due to the mixed-layer deepening and surface cooling (e.g., Kamidaira et al., 2018). Satellite ocean color images have proven that such mesoscale and submesoscale structures significantly affect the upper ocean dynamics to alter surface Chl-*a* concentrations at these scales (e.g., Sangrà, 2015; Hsu et al., 2020).

## 3.2 Comparison between Kuroshio Region and Kuroshio Extension Region

### 3.2.1 Vertical structures and eddy-driven nitrate flux

The surface Chl-*a* in Figure 2 shows noticeable differences in spatial patterns between the upstream (i.e., the KR; e.g., M1 along 138°E, Figure 1) and downstream (i.e., the KE; N1 along 145°E) regions along the Kuroshio. In the KR, a shoreward-confined high Chl-*a* is formed, compared with that in the KE. To understand the mechanisms of the different responses of primary production in the two regions, we investigated the

vertical structures across the Kuroshio path and at two locations ±0.8° away from the path (Figure 1). Note that the Kuroshio path is defined by the maxima of the surface current velocity. In the present model, we assume that the nitrogen source is distributed as nitrate in the subsurface, beneath the mixed-layer (Sec. 2). Figure 3 shows Hovmöller diagrams of the nitrate concentration (left column), phytoplankton concentration (middle column), and vertical eddy-induced nitrate flux (right column) in the northern, central, and southern sides of the Kuroshio, from the top to the bottom rows along 138°E (M1, Figure 1B) in the KR. The magenta lines indicate the corresponding mixed-layer depth determined by the KPP boundary-layer sub-model of ROMS. To examine the impacts of eddies on vertical nitrate transport, the vertical nitrate flux $F_V$ was evaluated by applying Reynolds decomposition of relevant variables into the mean and eddy components using the following equation:

$$F_V = Nw \approx \underbrace{\bar{N}\,\bar{w}}_{\text{mean}} + \underbrace{\overline{N'w'}}_{\text{eddy}}, \qquad (10)$$

where $w$ is the upward vertical velocity, $N$ is the nitrate concentration $[NO_3^-]$, the overbar denotes an ensemble (time) averaging operator, and the prime indicates the fluctuating (eddy) component for periods shorter than 90 days, calculated with a Butterworth frequency filter. Upward transport is defined as positive. We confirmed the cross terms are sufficiently small.

As expected, intra-annual, seasonal variability is evident in nitrate supply to the surface and the mixed-layer depth (Figures 3A-C). The mixed-layer deepens in colder seasons from December to April, along with an enhanced nitrate supply to the surface. This pattern is most significant on the
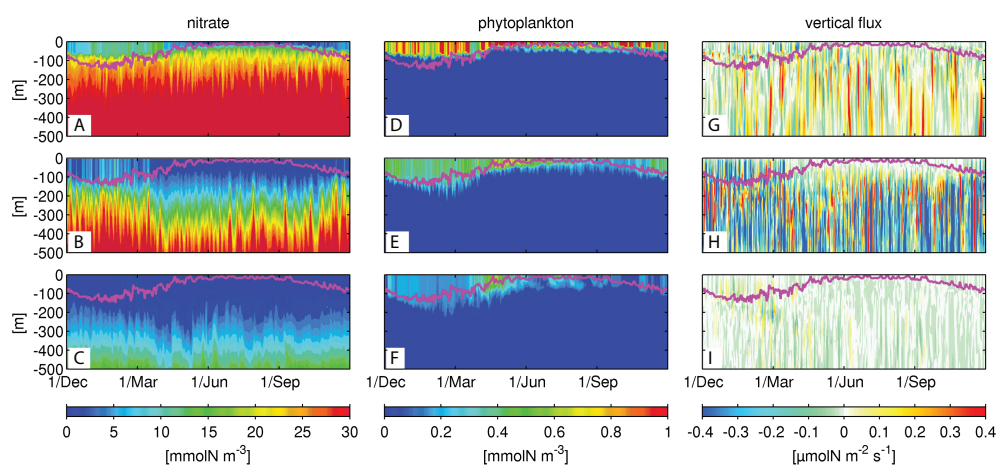


**FIGURE 3**
Hovmöller diagrams of nitrate concentrations (left column), phytoplankton concentration (middle column), and vertical eddy-driven nitrate flux (right column) in the northern (top row), central (middle row) and southern (bottom row) locations along 138°E in the Kuroshio Region (KR, M1 as shown in Figure 1). The magenta lines are the corresponding mixed-layer depth determined by the K-Profile Parameterization sub-model in ROMS.

northern side of the path in the KR, where nitrate concentration is the highest near the surface (Figure 3A). As the upper bound of the subsurface nitrate source (e.g., intermediate concentration at ~15 mmolN m$^{-3}$ depicted in cyan) is lowered in the southward direction, as represented from Figures 3A-C, a meridional transition occurs with a southward upper-ocean decline in nitrate concentration. Although the upper bound is elevated at the northern location in warmer seasons from May to October, surface nitrate concentration is as low (Figure 3A) as those at the central and southern locations where the warm season upper bound is lowered (Figures 3B, C). Phytoplankton (viz., Chl-*a* concentrations) fluctuates quite sensitively in response to fluctuations in nitrate concentration in the mixed-layer (Figures 3D-F), depending on nitrate concentrations and geographical locations relative to the Kuroshio axis. Chl-*a* is distributed much deeper in colder seasons than warmer seasons because of deep convective vertical mixing, indicated by deepening of the mixed-layer, that promotes upward entrainment of subsurface nutrient-rich water, thereby maintaining high productivity.

Figure 4 shows the same plots as Figure 3, but along 145°E (KE, N1 in Figure 1A) to represent the KE region. Similar to the KR in Figure 3, primary production is largest on the northern side of the Kuroshio, particularly in colder seasons with a southward meridional phytoplankton downgradient (Figures 4D-F), where the nitrate upper bound descends (Figures 4A-B), even at the same distances from the Kuroshio path as compared to those in the KR. The spring blooms occur along the Kuroshio path and its south side from April to May (Figures 3E-F), while at the northern location, Chl-*a* concentrations in colder seasons are occasionally as high as those in spring (e.g., Dec. 20 and Feb. 10 in Figure 3D). The vertical eddy-driven nitrate transport is positive (upward) in the

southern region. However, downward fluxes appear in the mixed-layer in winter along the Kuroshio path and its north side (Figures 3G, H), suppressing upper-ocean primary production associated with eddy influences.

Chl-*a* within and around the mixed-layer appears to be higher in the KE, exhibiting a reddish color from April to June (Figures 4E-F; up to ~1 mmol N m$^{-3}$) than that in the KR (Figures 3E-F; ~0.4 mmolN m$^{-3}$), except for the northern location where the nitrate concentration below the mixed-layer is much higher in the KR (Figure 3A). The spring bloom is also more remarkable in the KE than in the KR. The eddy-induced flux tends to exhibit upwelling at depths of ~100-300 m in the KE, particularly in colder seasons rather than warmer seasons, in the northern location (Figure 4G). As the sign of eddy nitrate flux fluctuates rapidly and repeatedly in time, we will look into time-averaged spatial distributions later. It should be noted that a high correlation (a correlation coefficient of ~0.62) between the nitrate concentrations and vertical eddy nitrate fluxes in both regions demonstrates that nitrate supply to the surface layer is strongly influenced by mesoscale and submesoscale eddies. Such a high correlation is more pronounced in the colder season, particularly on the north side of the Kuroshio path (Figures 3A and 4A). These results demonstrate that nutrient fluxes from the nutrient-rich subsurface layer to the nutrient-depleted surface layer are substantial for maintaining primary production near the surface.

The other biological components (zooplankton, ammonium, and detritus) are briefly described below with the supplemental Figures S1 and S2. Increase in zooplankton concentration on the north side of the Kuroshio is delayed for a month or two (Figures S1A and S2A) compared with phytoplankton concentration, while zooplankton concentration is fairly low along the Kuroshio path and its south side (Figures S1B-C and S2B-C).
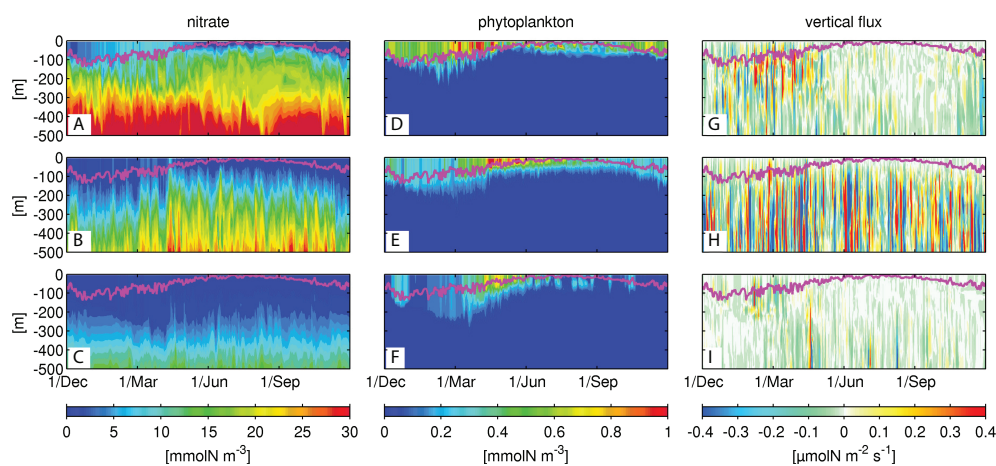


FIGURE 4
Same as Figure 3, but for 145°E in the Kuroshio Extension (KE, N1 as shown in Figure 1).

During the spring bloom, nitrate is mainly consumed by phytoplankton, which is subsequently grazed by zooplankton. Nitrogen is mostly stored in phytoplankton and zooplankton compartments in the KR and KE. Therefore, the nitrate concentration decreases significantly, exhibiting an obvious negative correlation between plankton and nitrate concentrations. Phytoplankton and zooplankton death further enriches detritus sinking to ~100 m from the base of the mixed-layer (Figures S1D-F and S2D-F). Hence, the detritus concentration is commonly distributed relatively deeper in colder seasons than in warmer seasons because of the enhanced vertical mixing in colder seasons. Detrital decomposition and zooplankton death concurrently contribute to the increase of ammonium concentrations. Hence, inorganic nitrogen deduced from detritus is the major source of ammonium in the deeper region below the mixed-layer, especially on the northern side. Uptake of both nitrate and ammonium by phytoplankton leads to the depletion of ammonium in the mixed-layer, particularly along the Kuroshio path and on the southern side. The ammonium and detritus concentrations are higher in the KE than in the KR. The largest difference between the two regions is the subsurface ammonium on the northern side, which is distributed to 300 m depth in the KE, while it exists down to ~100 m below the mixed-layer base (Figure S2G). In addition, high-frequency fluctuations associated with eddy-driven nutrient transport are significant in all these compartments, showing substantial impacts of eddies on the biogeochemistry to depths of several hundred meters.

### 3.2.2 Averaged horizontal structures of vertical eddy-induced nitrate flux

In the upper ocean, the transient (eddy) component of the vertical nitrate flux dominates over the mean flux, as mentioned later. Therefore, we computed the vertically integrated eddy-induced nitrate flux $F_v$ (Eq. 10) from the surface to a depth of 300 m to examine seasonal patterns of the horizontal distribution. We adapted 300 m here for the lower bound of the vertical integral in both seasons because it mostly encompasses highest productivity in winter (Figures 3 and Figure 4), whereas it shallows in summer that may lead to underestimation of $F_v$. However, this choice does not actually cause much problems according to our sensitivity tests with different depths for the lower bound. The upper panels of Figure 5 show the spatial distribution of vertically integrated and seasonally averaged $F_v$ for winter and summer, while the lower panels are the enlarged views of the KR, shown by the blue boxes in the upper panel. The mean eddy-induced nitrate flux is generally large around the Kuroshio path, with several sign changes occurring as the Kuroshio flows northeastward in both seasons. Downward (bluish colors; ~136°E–139°E & ~33° N–34°N; ~140°E–142°E & ~34°N–35°N) and upward (reddish
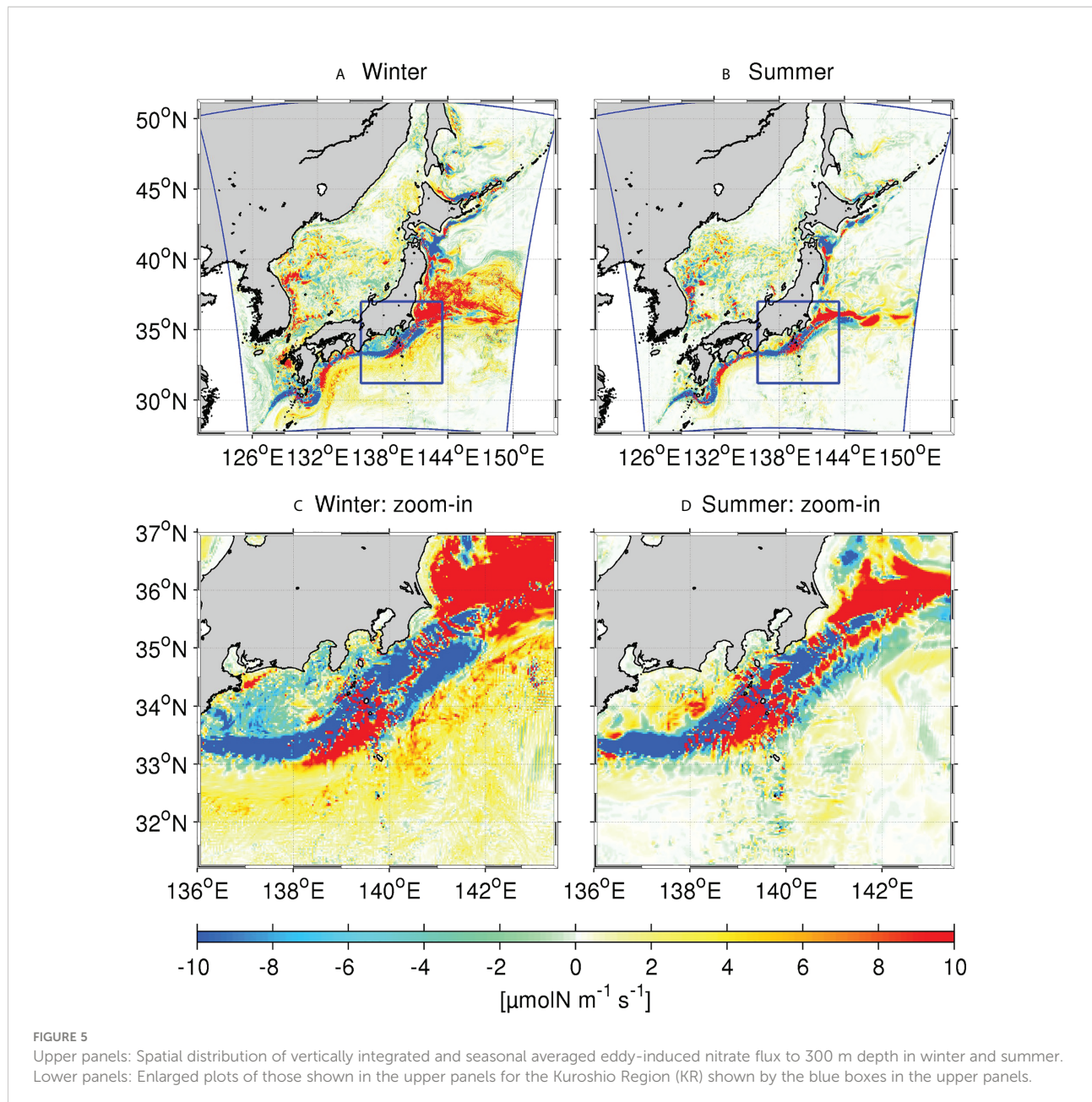
colors; ~138°E–140°E & ~33°N–34°N; <~141°E & <~35°N) fluxes alternately occur along the Kuroshio path, with an overall downward (upward) dominance in the KR (KE). Coastline topographies are also responsible for magnifying the eddy flux and enhance the complexity of the spatial distribution. The Enshunada Sea, located in the north of the Kuroshio in 136° E–140°E & 33.4°N–34.6°N, is characterized by a clear downward eddy flux in winter (Figures 5A, C), but by an overall positive (upward) flux in summer (Figures 5B, D).

Seasonal differences in vertical eddy-driven nitrate fluxes are also apparent. The magnitude and extent of influences are largely increased (decreased) in winter (summer) when vertical mixing is stronger (weaker). Focusing on differences in the KR and KE regions, we note that the major trend of eddy nitrate flux is negative (downward) in the KR, particularly in the Enshunada Sea in winter, which competes with coastal upwelling nitrate transport from the nutrient-rich subsurface water as downward nitrate flux serves to reduce productivity. The spatially averaged eddy flux in the KR is dominated by downward flux, except during summer because of the intensive subsurface downward flux underneath the Kuroshio axis, as illustrated by the prominent negative flux in Figure 5 (see also Uchiyama et al., 2017). In contrast, the eddy nitrate flux is broadly positive (upward) in the KE (Figure 5A), particularly during winter, while it is negligibly small north of the Kuroshio during summer (Figure 5B). The sign change occurs around the Izu-Ogasawara Ridge, where the negative downward eddy flux in the upstream region (<139°E) becomes positive over the ridge (139°E–140°E), and then reverts back to negative in the downstream (140°E– 142°E), before reaching the KE, particularly in winter.

## 3.3 Effects of the oceanic ridge in the Kuroshio Region: island mass effects

The Kuroshio flows over an oceanic ridge (Izu-Ogasawara Ridge; Figure 1B), located on the south coast of Japan in the KR, meridionally stretching along 139–140°E. This unique topography is considered to have remarkable influences on the Kuroshio and eddies, further affecting the associated biogeochemical responses. To examine changes in biogeochemistry due to the ridge, we set four more cross-sections along 138.9°E, 139.7°E, 140.5°E, and 141.4°E, both upstream and downstream of the ridge (M2-5, Figure 1B).

Figure 6 illustrates Hovmöller diagrams of nitrate concentrations on the time-averaged Kuroshio main axis, from west to east, and the two meridionally remote stations ±0.8° from the axis. The sampled stations represented by black dots in Figure 1B were selected on the M2-5 transects. Sets of the three vertically aligned panels, for example, Figures 6M2a-c (for M2), are similar to Figures 3A-C (for M1). Note that the depths at the northern stations along M3 and M4 are ~300 m, and thus the data below that depth are null. In addition, the northern station

**FIGURE 5**
Upper panels: Spatial distribution of vertically integrated and seasonal averaged eddy-induced nitrate flux to 300 m depth in winter and summer.
Lower panels: Enlarged plots of those shown in the upper panels for the Kuroshio Region (KR) shown by the blue boxes in the upper panels.

along M4 is so close to the shore, with a depth of ~100 m, that it was replaced by a slightly offshore station at +0.4° (not +0.8°) from the Kuroshio path. Figures 7, 8 show the same sets of plots as Figure 6 but present phytoplankton concentrations (Figure 7) and upward positive vertical eddy nitrate fluxes $F_v$ (Figure 8).

The general structure and variability are similar to those along M1, as discussed in Section 3.2.1. For instance, the mixed-layer deepens in colder seasons, thereby promoting nitrate supply to the surface layer from the subsurface at all stations except for the northern station along M5 (Figure 6M5A), where nitrate concentration varies intermittently in the upper 300 m layer, with a longer fluctuation period, presumably as a result of

the reduced topographic constraint, to be a more freely fluctuating Kuroshio jet. Chl-*a* concentrations are also highest in the northern stations with prominent spring blooms in Apr.–Jun. (Figure 7M5A), consistent with the increased nitrate distributions, with a lag of a few months. A strong eddy nitrate flux occurs in the mixed-layer during the colder season (Dec.–Apr.), followed by enhanced flux mainly below the mixed-layer, but extended to the surface layer in the subsequent spring (Apr.–Jun.). Therefore, the increased vertical mixing due to surface cooling in winter promotes upper-ocean eddy nitrate fluxes, bringing subsurface nitrate to the surface layer persistently for a few months, which preconditions the
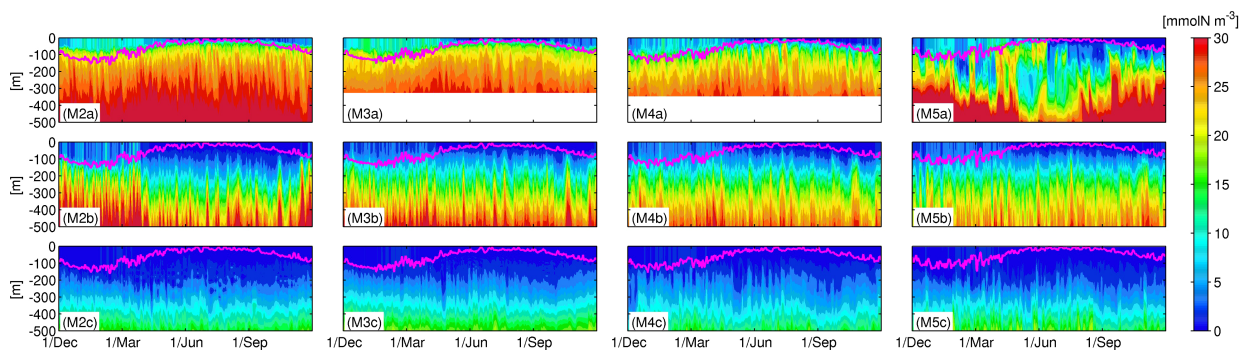
FIGURE 6

Hovmöller diagrams of the nitrate concentrations in the northern (top row), central (middle row) and southern (bottom row) locations represented by black dots Figure 1B along M2-5 in the KR. The magenta lines denote the corresponding mixed-layer depth.

subsequent Chl-*a* bloom under optimal radiation conditions in spring. During the spring bloom, the near-surface nitrate is consumed by phytoplankton, leading to a depletion.

The ridge area (M3) is demonstrated to significantly alter the nitrate distribution, where the near-surface nitrate is moderately higher downstream compared to the upstream region, especially at the northern stations (Figures 6M2a-M5a). Phytoplankton is distributed shallower in the upstream region, but is distributed below the mixed-layer at a depth of ~200 m in the downstream region. By contrast, at stations on the Kuroshio (Figures 6M2b-M5b), near-surface nitrate concentration is higher in the upstream region, while subsurface nitrate is lower, leading to steeper vertical nitrate gradients in the upstream region than downstream. Such an increase in the vertically extended nitrate gradation in the downstream region is also visible at the depths of ~100–300 m at the southern stations (Figures 6M2c-M5c). Upper-ocean Chl-*a* is distributed consistently with the vertically elongated nitrate, leading to increased thickness of the high Chl-*a* water towards

the downstream region at the central and southern stations. Primary production appears in spring along the eastern-most transect (Figures 7M5a-M5c), although the nitrate concentration is relatively low (Figures 6M5a-M5c), again perhaps due to the nature of the Kuroshio jet that could promote abrupt vertical flux and horizontal nitrate transport from the upstream region (e.g., Nagai et al., 2019), thereby enhancing the production of phytoplankton. Eddy-driven nitrate flux is the strongest along the main axis (Figures 8M2b-M5b), exhibiting considerable vertically elongated structures, demonstrating the predominance of quasi-geostrophic mesoscale eddies, especially around the oceanic ridge (Figure 8M3b). In turn, enhanced eddy fluxes in the mixed-layer in colder seasons indicate the emergence of susbmesoscale eddies, which can be marginally resolved in the present ROMS model (see Figure 2). Hence, the influence of mesoscale eddies is most apparent on the Kuroshio path, near the ridge, and within the downstream region on the north side of the path, where the vertical Chl-*a* gradient is less obvious. For
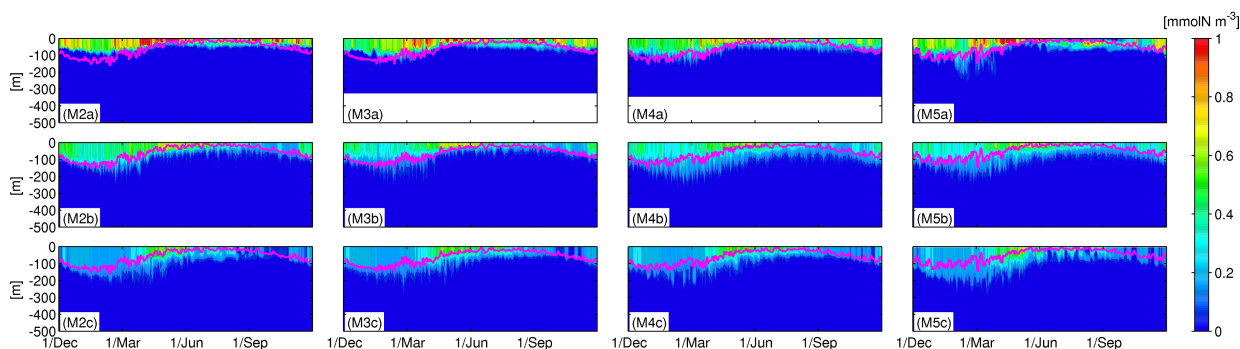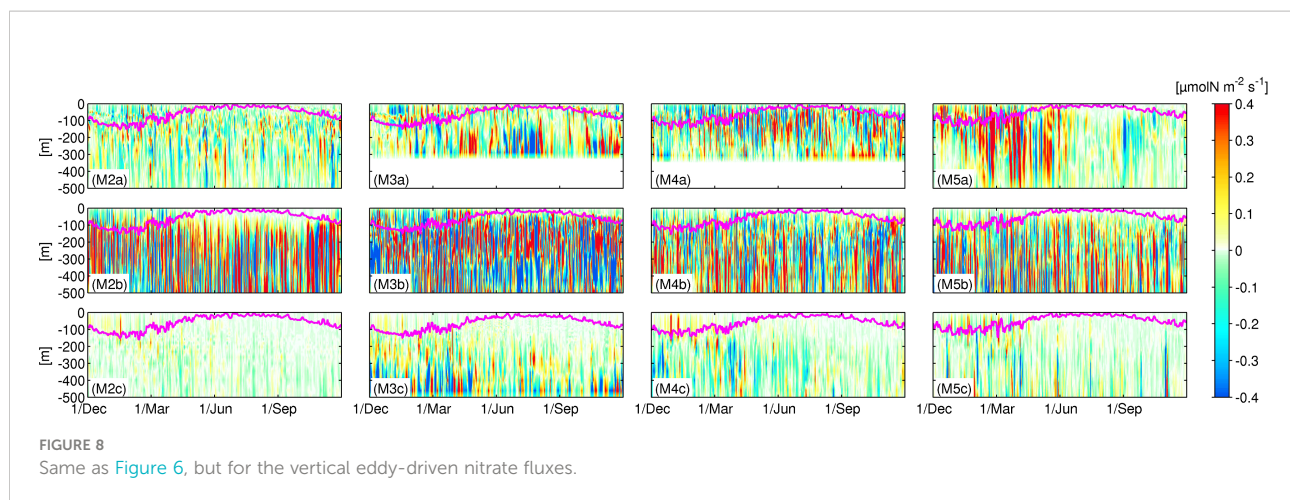


FIGURE 7

Same as Figure 6, but for the phytoplankton concentrations.

**FIGURE 8**
Same as Figure 6, but for the vertical eddy-driven nitrate fluxes.

example, in winter and spring, the vertical eddy flux is larger at the northern station in the downstream (Figure 8M5a) than that in the upstream (e.g., Figure 8M2a) according to both mesoscale and submesoscale eddies that sustain local upwelling of nitrate, resulting in surface-concentrated high nitrate (Figure 6M5a) and subsequent spring blooms (Figure 7M5a).

# 4 Discussion

## 4.1 Eddy generation mechanisms

To investigate the generation mechanism of eddies that play a central role in stimulating eddy nitrate fluxes, we assessed the energy conversion terms relevant to eddy kinetic energy (EKE). We focus on $K_m K_e$, the conversion of mean kinetic energy to eddy kinetic energy due to shear instability, and $P_e K_e$, the conversion of eddy potential energy to eddy kinetic energy due to baroclinic instability, as defined by the following equations (e.g., Klein et al., 2008; Oey, 2008):

$$K_m K_e = -\left( \overline{u'u'} \frac{\partial \bar{u}}{\partial x} + \overline{u'v'} \frac{\partial \bar{u}}{\partial y} + \overline{u'w'} \frac{\partial \bar{u}}{\partial z} + \overline{v'u'} \frac{\partial \bar{v}}{\partial x} + \overline{v'v'} \frac{\partial \bar{v}}{\partial y} + \overline{v'w'} \frac{\partial \bar{v}}{\partial z} \right), \quad (11)$$
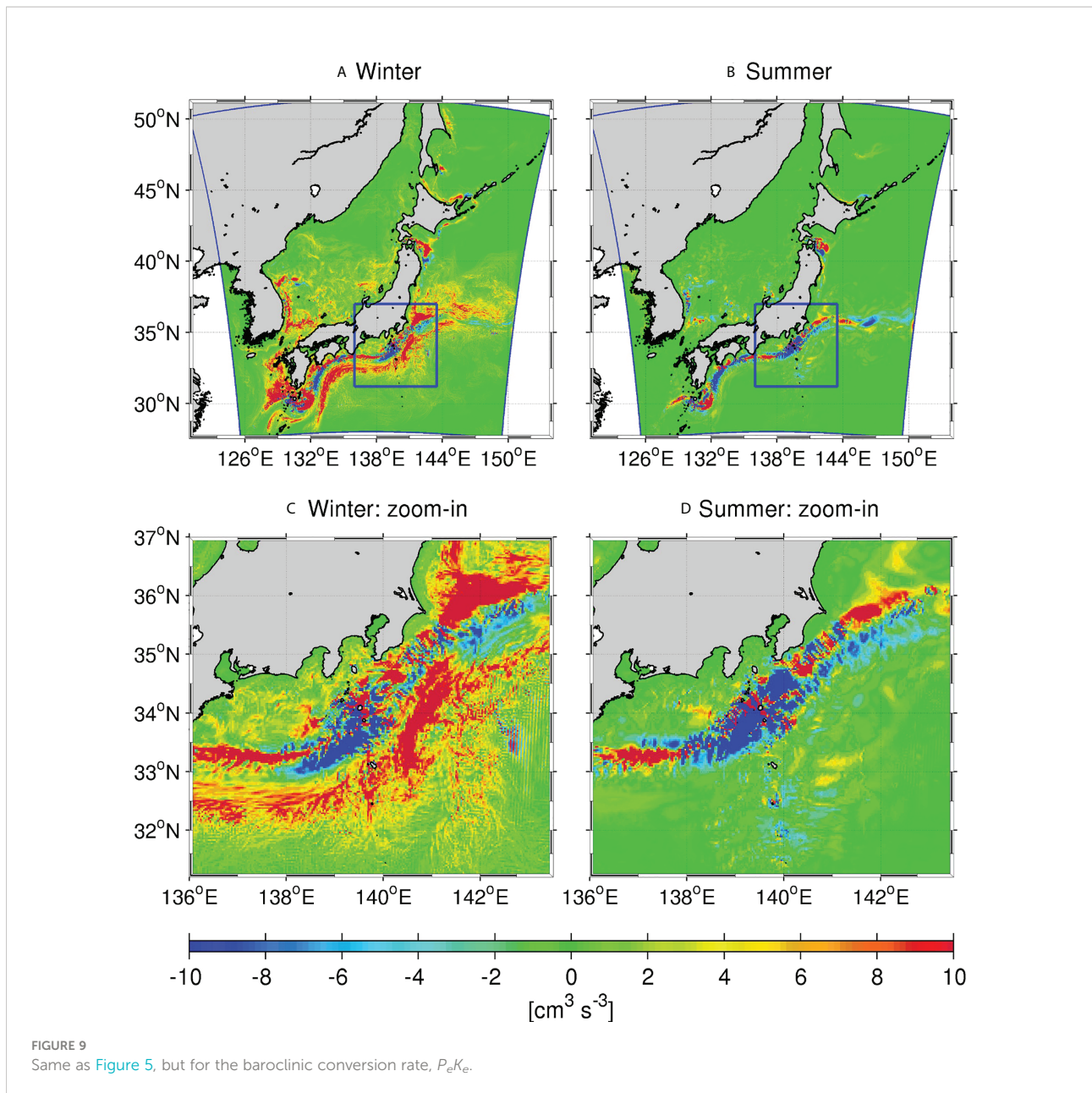
$$P_e K_e = -\frac{g}{\rho_0} \overline{\rho' w'}, \quad (12)$$

where $(x,y,z)$ are the horizontal and vertical coordinates, $u$ and $v$ are eastward and northward horizontal velocities, $P$ is the density of sea water, $P_0 = 1025.5 \text{kg m}^{-3}$ is the reference density, and $g$ is the gravitational acceleration. As $K_m K_e$ and $P_e K_e$ are dominant source terms in the EKE conservation equation, EKE is increased (decreased) to let the mean flow be unstable (stable) when $K_m K_e$ and $P_e K_e$ are positive (negative).

Figure 9 is the same set of plots as Figure 5, but shows the horizontal distributions of vertically integrated $P_e K_e$ to a depth of 300 m in two seasons. Positive $P_e K_e$ is distributed broadly

along the Kuroshio path in winter (Figures 9A, C), consistent with previous studies (e.g., Sasaki et al., 2014; Uchiyama et al., 2017; Kamidaira et al., 2018), which suggested that surface cooling and associated mixed-layer deepening give rise to baroclinic instability, resulting in the generation of vigorous mesoscale and submesoscale eddies much more extensively in colder seasons in this area. The enhanced vertical eddy-driven nitrate flux in winter shown in Figures 5A, C is generally collocated with the areas where large positive $P_e K_e$ is distributed. In contrast, $P_e K_e$ decreases to narrow to the Kuroshio path and is largely negative in summer (Figures 9B, D), resulting in reduced eddy intensity; the vertical eddy nitrate flux is reduced accordingly (Figures 5B, D). In the KR, negative $P_e K_e$ appears near the Izu-Ogasawara Ridge in both seasons. This ridge has a unique topographic feature, consisting of many islands and submerged seamounts, with depths shallower than 1000 m. Therefore, the ridge is considered to interact with the Kuroshio even at depths of ~800–1000 m (Figure 10), which influences subsurface water to a depth of 1000 m in the KR, sometimes called island mass effects. Further analyses of the influence of the ridge will be provided in the subsequent section. It must be noted that the horizontal distribution of $K_m K_e$ is more or less similar to the distribution of $P_e K_e$ in winter, with almost no clear seasonal variability, and is therefore not shown here.

To highlight the differences between the two EKE source terms in the KR and KE regions, cross-sectional plots of seasonally averaged $K_m K_e$ (upper panels) and $P_e K_e$ (lower panels) in winter along 138°E (KR; M1 in Figure 1) and 145°E (KE; N1 in Figure 1) are shown in Figure 10. The associated mixed-layer depth is depicted by magenta lines. The black dotted contours are the eastward velocity normal to the cross-sections, representing the Kuroshio main body. In the KR, eddies are generated by a combination of the positive $K_m K_e$ and $P_e K_e$ around the Kuroshio path in the upper ocean, while $P_e K_e$ prevails over $K_m K_e$ within the mixed-layer, extending to ~32.1°N on the southern side of the path, as well as up to the coastline at ~34.6°N to

**FIGURE 9**
Same as Figure 5, but for the baroclinic conversion rate, $P_eK_e$.

the north, to a lesser degree (Figures 10A, B). Therefore, shear instability (positive $K_mK_e$) due to the energetic Kuroshio mainly promotes mesoscale eddies near the path (e.g., ~32.9°N–33.6°N & 138°E) that leads to negative downward eddy-driven nitrate flux in the KR, i.e., the downstream region of the ridge, in winter (bluish areas: ~136°E–139°E & ~33°N–33.5°N, ~140°E–142°E & 33.5°N–35° N. Figures 5A, C). Baroclinic instability (positive $P_eK_e$) in winter is also important to the broadly distributed high EKE off the path, resulting in the downward $F_v$ near the coast to the north (~136°E–140°E & ~33°N–34.5°N), and the upward $F_v$ to the south (>~33°N) in the mixed-layer (Figure 5C).

In contrast, in the KE region, the positive $K_mK_e$ and $P_eK_e$ (Figures 10C, D) jointly give rise to upward eddy nitrate flux

(Figure 5A) in the upper ocean in winter along the N1 transect, maintaining near-surface primary productivity. Similar to the KR, shear instability occurs only near the Kuroshio, whereas baroclinic instability is extensive along the meridional length more evidently on the north side of the path, thereby promoting eddy intensity and increased upward eddy flux due to vigorous vertical mixing that bring the subsurface nitrate to the upper ocean, even away from the path. This meridional asymmetry of $P_eK_e$ distributions is key to the more active primary production occurring broadly in the KE around the Kuroshio path and its northern region in winter (Figure 5A), despite the upper bound of the subsurface nitrate source being located deeper in the KE (Figure 4), than in the KR (Figure 3).
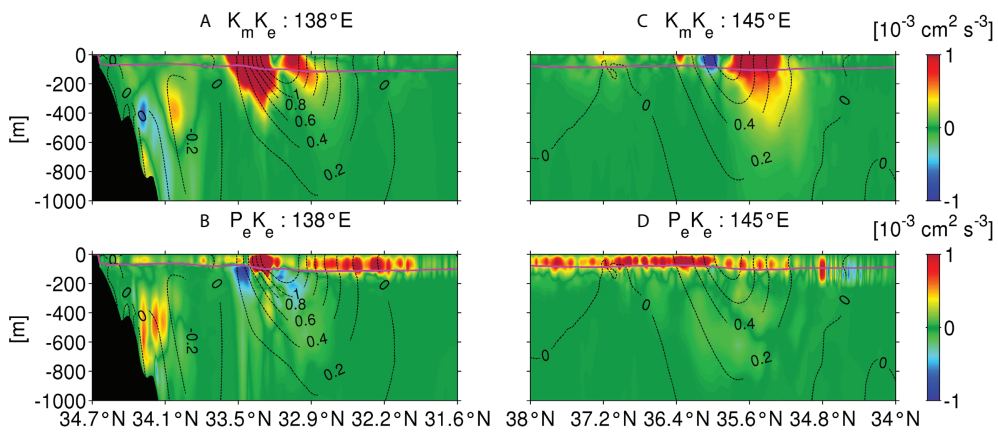
**FIGURE 10**
Cross-sectional plots of the seasonally averaged barotropic conversion rate, $K_m K_e$ (top row), and baroclinic conversion rate, $P_e K_e$ (bottom row), along 138°E (M1) in the KR (left column) and 145°E (N1) in the KE (right column) in winter. The magenta lines denote the mixed-layer depth computed by KPP model. The black dotted contours show eastward velocity perpendicular to the transects, denoting approximate positions of the Kuroshio.

Figure 11 shows the same plots as Figure 10, but in summer. Compared to winter, the surface mixed-layer becomes thinner in summer, clearly reducing baroclinic instability as $P_e K_e$ is only significant near the Kuroshio path in both KR and KE regions. The summer $K_m K_e$ is similarly distributed to that in winter, with almost no obvious seasonal variability, as mentioned earlier in this subsection. In the KR, positive $P_e K_e$ (Figure 11B) promotes the eddy-driven downward nitrate flux (Figure 5B) through baroclinic instability only near the Kuroshio path (~136°E–139°E & ~33°N–33.5°N) in summer, although positive $P_e K_e$ in the mixed-layer in winter (Figure 10B) is attributed to the much wider appearance of non-trivial eddy fluxes $F_v$ (Figure 5B). Likewise, in the KE, $P_e K_e$ is considerably diminished,

becoming negligible, while the development of positive $K_m K_e$ near the path plays a role in maintaining modest eddy nitrate flux in this location. A sign of $F_v$ largely depends on the background nitrate distribution; $F_v > 0$ (upward) occurs if eddy mixing reaches down to the subsurface nitrate reservoir, otherwise $F_v < 0$ (downward) or if near-surface nitrate supply is expected in case of coastal upwelling etc.

In summary, baroclinic instability is the most important factor accounting for seasonal variability in eddy generation. It vitally stimulates the downward and upward eddy-induced nitrate fluxes in the upper ocean in the KR and KE in winter, while its influence becomes much weaker in both regions in summer.
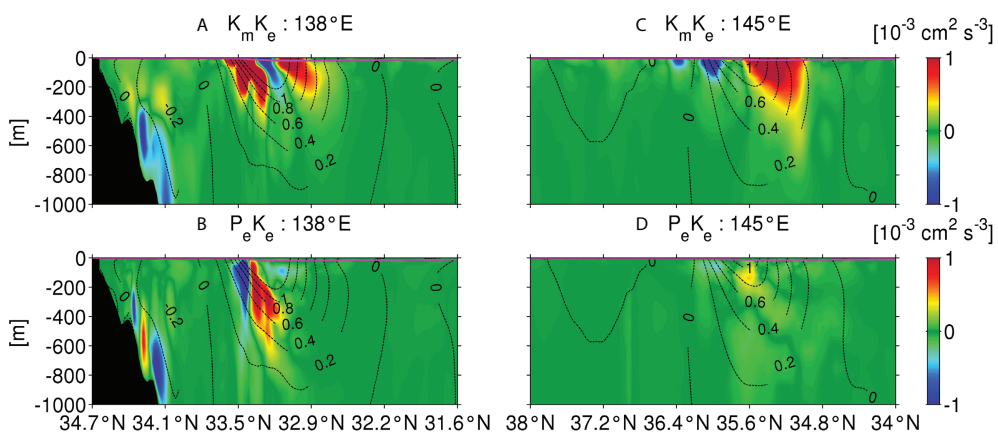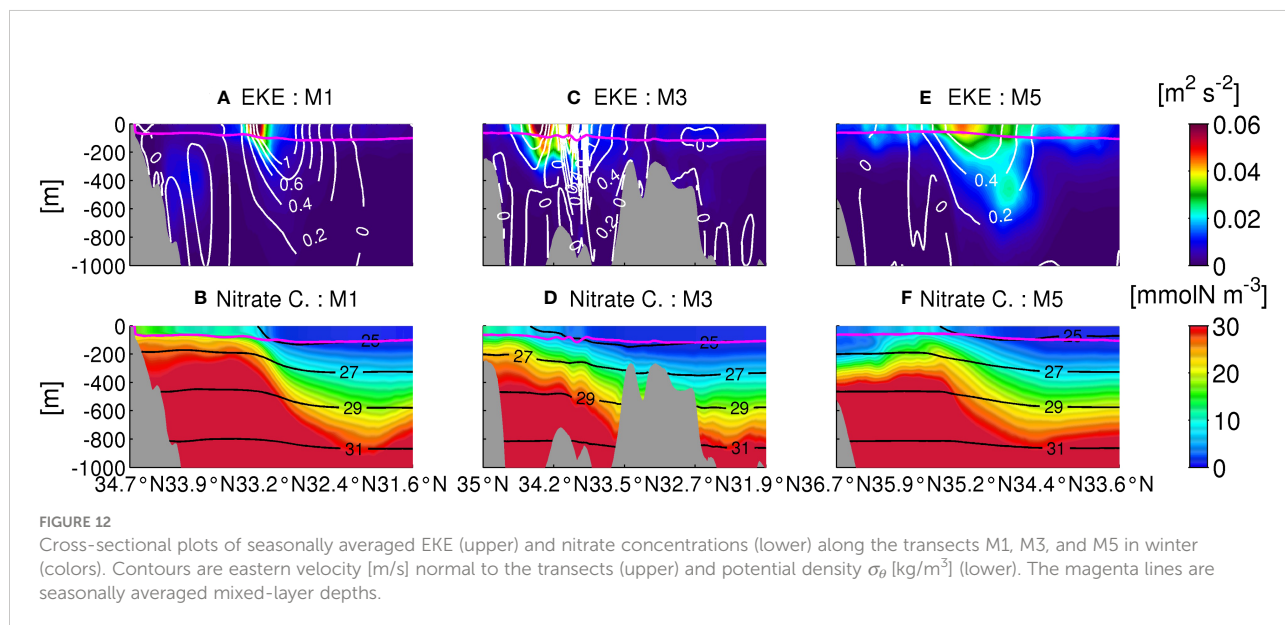


**FIGURE 11**
Same as Figure 10, but in summer.

## 4.2 Altered dynamics around the oceanic ridge

To investigate a possible mechanism responsible for spatial changes in vertical nitrate transport in the KR, we examined the cross-sectional distributions of seasonally averaged values of several variables in winter (Dec.–Feb.) along the three transects (M1, M3, and M5, Figure 1B) in Figure 12 (more detailed spatial structures are shown in Figure S3). The displayed variables are EKE = ( $= \frac{1}{2}(\overline{u'^2} + \overline{v'^2})$, colors) and eastward horizontal velocity normal to the transects (white contours) in the upper panel, while nitrate concentrations (colors) and potential density $\sigma_\theta$ (black contours) are shown in the lower panels. The magenta lines are the seasonally averaged mixed-layer depth estimated by the KPP model. The Kuroshio main body is inclined to extend southward to ~800 m depth. It is shaped by topographic influences of the ridge near M3, as shown in Figure 12C. EKE peaks near the surface and slightly northward of the maximum velocity of the Kuroshio, in conjunction with the maximum horizontal velocity shear, with magnified complexity exhibited by two EKE peaks around the ridge at ~34.4°N and ~33.7°N (Figure 12C). Similarly, nitrate concentration and potential density are also inclined southward, with elevated values near the coast inducing northward upwelling of subsurface nitrate and potential energy from the base of the Kuroshio main body to the coast. Mixed-layer depth is consistently shallower on the shore side than offshore (magenta lines in Figure 12). Near-surface nitrate is higher in the upstream region, whereas elevated nitrate does not reach the coast along M5 (Figure 12F). The concentrated EKE peak along M1 spreads meridionally in the upstream, while it is decreased

and distributed not only near the surface but also at depth, downstream along M5. A simple but plausible description of the dynamical effects of the ridge on the Kuroshio and associated eddy activity is a squashing by islands and submerged seamounts, as illustrated in Figures 12C, D, which spontaneously accelerates and occasionally bifurcates the Kuroshio, amplifies the lateral velocity shear, and promotes mesoscale eddies around the topographies, even at depth. Such enhanced mesoscale eddies shed by the ridge make vertical and horizontal mixing more energetic, thereby inducing vertically extended intensive eddy flux (Figure 11M3c). After passing over the ridge, the squashed Kuroshio is relaxed to expand laterally downstream, resulting in deceleration of the Kuroshio main body and reduced eddying fluctuations spreading over wider and deeper areas (see Figures 12A, E).

It is noteworthy that the seasonal variability in these cross-sectional structures is insignificant, except for a minor meridional shift of the Kuroshio path up to ~0.4°, and a shallower mixed-layer, particularly in summer, as supplemented in Figure S4. As shown in Figures 2 and Figure 11, the deepened mixed-layer is accompanied by energetic submesoscale activities occurring mostly within the mixed-layer in colder seasons, which are attributed to additional near-surface eddy nitrate fluxes that promote upward nutrient supply through enhanced vertical mixing. These submesoscale eddies are primarily provoked by baroclinic and mixed-layer instabilities, triggered by surface cooling and down-front wind, which makes the Ertel potential vorticity negative and preconditions symmetric instability in the upper ocean (Thomas and Lee, 2005; Thomas and Taylor, 2010; Kamidaira et al., 2018; Nagai et al., 2019), regardless of the ridge topographies.



**FIGURE 12**
Cross-sectional plots of seasonally averaged EKE (upper) and nitrate concentrations (lower) along the transects M1, M3, and M5 in winter (colors). Contours are eastern velocity [m/s] normal to the transects (upper) and potential density $\sigma_\theta$ [kg/m$^3$] (lower). The magenta lines are seasonally averaged mixed-layer depths.
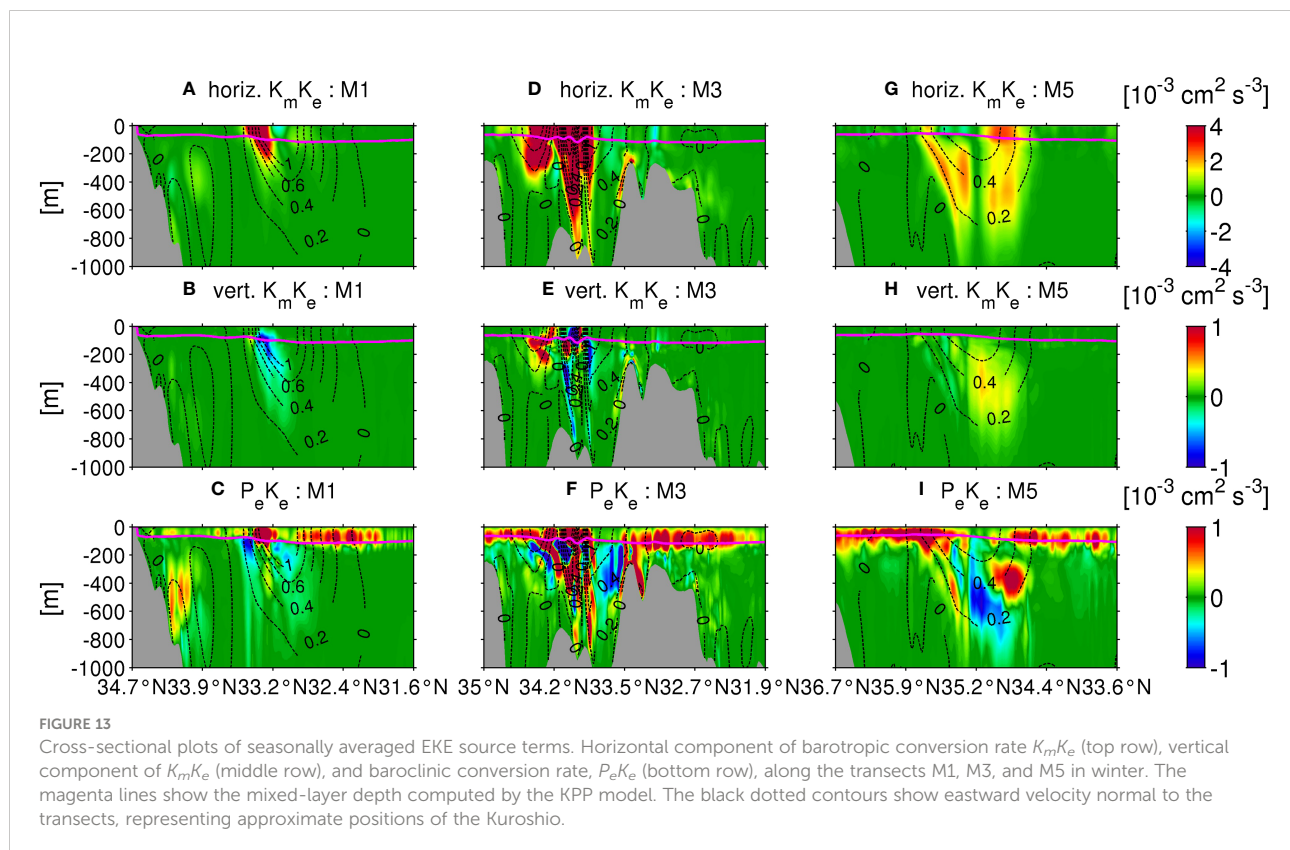
## 4.3 Eddy generation by the oceanic ridge

Thus far, we have understood that spontaneous generation of mesoscale eddies by the Kuroshio shear and submesoscale eddies by surface cooling are the two substantial elements that affect eddy nitrate fluxes responsible for sustaining primary production in the KR and KE regions. An additional key mechanism may be the topographically-generated mesoscale variability due to the ridge. Therefore, we next examined the influences of the local topography on eddy generation by decomposing the barotropic conversion rate $K_mK_e$ into horizontal and vertical components, as well as the baroclinic conversion rate $P_eK_e$ along the three transects (M1, M3, and M5, Figure 1B) in winter (Figure 13) (more details are supplemented in Figure S5). Consistent with the mean variables in Figure 12, an apparent spatial asymmetry in the conversion rates is observed between the upstream and downstream regions, with respect to the ridge (M3; Figures 13D-F) as a pivot. In the upstream region, the positive horizontal $K_mK_e$ and $P_eK_e$ due to horizontal shear instability and baroclinic instability that concurrently induce eddy-driven nitrate flux near the Kuroshio. Positive $P_eK_e$ is induced in the upper ocean due to submesoscale eddies, particularly near and on the south side of the path, with significant amplification in the downstream region, where the near-surface $P_eK_e$ is strengthened broadly to

extend on the north side of the Kuroshio. The vertical $K_mK_e$ is largely centered on the path and near the topography but is mostly negative or weak (notice the different scales), indicating that horizontal shear instability dominates over the vertical shear instability. All three conversion rates are significantly energized along M3 (139.7°E) around the ridge. When the Kuroshio passes over the ridge, it is squashed to enhance the horizontal velocity shear and subsequent eddy shedding, mostly at mesoscale, except for the upper ocean, where baroclinic submesoscale instability takes over shear instability, as anticipated in the preceding subsection. Moreover, an interaction between ridge topography and the Kuroshio front at depth triggers pronounced baroclinic instability below the mixed-layer along M3 (Figure 13F), leading to continuous subsurface destabilizing effects downstream (Figure 13I), with increased subsurface EKE (Figure 12E). Therefore, the deeper ocean is influenced by a combination of horizontal shear instability and baroclinic instability, provoking significant mesoscale eddy-driven nitrate transport downstream (Figures 8M4b, M5b), particularly on the northern side of the path (Figures 8M4a, M5a).

We should mention the distributions of conversion rate in warmer seasons (data not shown). Similar to the mean structures discussed in Section 4.2, the surface mixed-layer becomes thinner, resulting in considerable weakening of the near-surface submesoscale baroclinic instability. In addition to the



FIGURE 13
Cross-sectional plots of seasonally averaged EKE source terms. Horizontal component of barotropic conversion rate $K_mK_e$ (top row), vertical component of $K_mK_e$ (middle row), and baroclinic conversion rate, $P_eK_e$ (bottom row), along the transects M1, M3, and M5 in winter. The magenta lines show the mixed-layer depth computed by the KPP model. The black dotted contours show eastward velocity normal to the transects, representing approximate positions of the Kuroshio.

modest northward shift of the Kuroshio path that culminates with the northward shift of the subsurface peak location of $P_eK_e$ along M2, the overall patterns of the three conversion rates are predominantly the same as those for winter (Figure 13). However, the subsurface horizontal $K_mK_e$ and $P_eK_e$ are less significant or even negative (for $P_eK_e$, *i.e.*, stabilizing effects) in the downstream region, particularly along M5 in warmer seasons. Thus, the eddy fluxes are weakened (Figures 8M5a-c). Consequently, warmer seasons are characterized by a modest northward shift of the Kuroshio by ~0.4° in the present climatological model results. This subtly affects changes in the conversion rates, whereas the interaction between the Kuroshio and the ridge topography is crucial to alterations in eddy intensity in the downstream region. In turn, the warmed upper ocean and increased incoming surface heat and radiation fluxes greatly suppress near-surface submesoscale fluctuations, which resulted in reduced vertical mixing, eddy nitrate fluxes, and thus primary production in the upper ocean in warmer seasons.

# 5 Concluding Summary

The Kuroshio has been recognized as a nutrient stream that supplies nutrient-rich subsurface water to the upper ocean, most effectively by vertical eddy-driven nitrate fluxes (e.g., Uchiyama et al., 2017; Nagai et al., 2019). In the present study, we investigated seasonal variability of eddy fluxes that sustain upper ocean primary production, and the driving mechanisms behind them in the Kuroshio Region (KR) and Kuroshio Extension (KE) regions off the Pacific coast of Japan by using the JCOPE2-ROMS downscaling circulation modeling suite coupled with an NPZD biogeochemical model. The upper-ocean primary production is found to be maintained by two completing effects associated with oceanic eddies: 1) the downward eddy nitrate flux that suppresses the production by near-surface nitrate extraction, and 2) the upward eddy nitrate flux that promotes the production by localized upwelling of the subsurface nutrients. The balance between these two effects varies with seasons and areas due to the different eddy generation mechanisms. In addition, we showed the shallow topography of the Izu-Ogasawara Ridge, which lies underneath the Kuroshio path, alters the eddy generation mechanisms significantly.

We paid a particular attention to surface chlorophyll-*a* (Chl-*a*) as the most important indicator of the upper-ocean primary production. Its distributions demonstrated that the segmentations in primary productivity occurred on both sides of the Kuroshio, with a higher Chl-*a* concentration in the northern area. An obvious spring bloom occurred on the northern side of the KE and on the main path of the Kuroshio. Enhanced vertical mixing in winter and subsequent improvement of the light environment in spring resulted in enhanced primary production around the Kuroshio, both in the KR and KE. The overall upward entrainment from the

nutrient-rich subsurface to the nutrient-exhausted surface is important for maintaining near-surface primary productivity. However, downward eddy nitrate fluxes were apparent in winter in the upstream (Enshu-nada Sea region) and downstream regions, relative to the ridge in the KR. Eddy generation analysis indicated that, in winter, the topographic eddy shedding, positive barotropic conversation rate ($K_mK_e$), and baroclinic conversion rate ($P_eK_e$) jointly promoted eddy-driven downward nitrate fluxes through shear and baroclinic instabilities most vigorously in the mixed-layer along the Kuroshio path and its northern side in the KR, which eventually suppressed biological productivity. Positive $P_eK_e$ leads to a relatively weak upward nitrate flux that maintained primary production on the southern side. In the KE, upward eddy flux, due to the combination of positive $K_mK_e$ and $P_eK_e$, enhanced primary production in the upper ocean. Influences of submesoscale eddy-driven, near-surface baroclinic instability extends broadly in the meridional direction, with a southward bias in the upstream region, and a northward bias in the downstream region, attributed to the spatially heterogeneous Chl-*a* distributions. By contrast, in summer, the mixed-layer depth became very shallow, and thus the upper ocean $P_eK_e$ almost vanishes in both KR and KE. Positive $K_mK_e$ and $P_eK_e$ arise mostly at depth beneath the mixed-layer, which strongly interacted with the ridge topography in the KR, increasing in the upstream region and decreasing in downstream region. In the KE, as $P_eK_e$ was prominently reduced in summer, eddy nitrate flux decreased significantly, particularly in the north of the Kuroshio. Therefore, baroclinic instability is the key influencer on seasonal variability in eddy generation near the surface, where vertical eddy mixing is inevitably important to promote subsurface nutrient supply to the upper ocean.

In terms of the topographic influences of the Izu-Ogasawara Ridge, one essential regional difference is that the spatial variability of the vertical eddy nitrate flux fluctuates more in KR than in KE. The spatial variability of the eddy-driven nitrate flux, and the underlying eddy generation mechanism, are significantly altered by ridge topography, characterized by flow squash and mesoscale eddy shedding. Turbulence associated with the Kuroshio tends to be less energetic in the upstream, while the ridge generates intensive eddy mixing more broadly and deeply in the downstream, mainly due to the interaction between the Kuroshio front and ridge topography, which results in mesoscale eddy-generating baroclinic instability. Although the near-surface nitrate concentration is lower in the downstream, the upward eddy-driven nitrate flux is stronger in maintaining primary production due to shear and baroclinic instabilities in winter. Quantitative comparison among the three major EKE source terms demonstrated that $P_eK_e$ and the horizontal $K_mK_e$ dominate over vertical $K_mK_e$ on eddy generation in the KR. The horizontal $K_mK_e$ increased in the Kuroshio path and the region near the ridge, while $P_eK_e$ was intense and highly variable in time in the mixed-layer. The seasonal meridional shift in the Kuroshio path was observed in

the present model, which introduced changes in the interaction between the ridge and the front responsible for $P_eK_e$ on an intra-annual time scale.

## Data availability statement

The original contributions presented in the study are included in the article/Supplementary Material. Further inquiries can be directed to the corresponding author.

## Author contributions

XZ: investigation, software, validation, visualization, and writing – original draft. YU: conceptualization, methodology, supervision, software, writing - reviewing and editing, and funding acquisition. EM: investigation. YS: investigation, software, and validation. HY: methodology and investigation. All authors contributed to the article and approved the submitted version.

## Acknowledgments

## Conflict of interest

YS and HY are employed by Construction Technique Institute Engineering Co., Ltd. and Alpha Hydraulic Engineering Consultants Co. Ltd., respectively.

The remaining authors declare that the research was conducted in the absence of any commercial or financial relationships that could be construed as a potential conflict of interest.

## Publisher's note

All claims expressed in this article are solely those of the authors and do not necessarily represent those of their affiliated organizations, or those of the publisher, the editors and the reviewers. Any product that may be evaluated in this article, or claim that may be made by its manufacturer, is not guaranteed or endorsed by the publisher.

## Supplementary material

The Supplementary Material for this article can be found online at: https://www.frontiersin.org/articles/10.3389/fmars.2022.990559/full#supplementary-material

## References

Ardyna, M., Babin, M., Gosselin, M., Devred, E., Bélanger, S., Matsuoka, A., et al. (2013). Parameterization of vertical chlorophyll *a* in the Arctic ocean: impact of the subsurface chlorophyll maximum on regional, seasonal and annual primary production estimates. *Biogeosci. Discuss.* 10, 1345–1399. doi: 10.5194/bgd-10-1345-2013

Ballantyne, A. P., Alden, C. B., Miller, J. B., Tans, P. P., and White, J. W. C. (2012). Increase in observed net carbon dioxide uptake by land and oceans during the past 50 years. *Nature* 488, 70–73. doi: 10.1038/nature11299

Bauer, J. E., Cai, W., Raymond, P. A., Bianchi, T. S., Hopkinson, C. S., and Regnier, P. A. G. (2013). The changing carbon cycle of the coastal ocean. *Nature* 504, 61–70. doi: 10.1038/nature12857

Becker, J. J., Sandwell, D. T., Smith, W. H. F., Braud, J., Binder, B., Depner, J., et al. (2009). Global bathymetry and elevation data at 30 arc seconds resolution: SRTM30_PLUS. *Mar. Geod.* 32 (4), 355–371. doi: 10.1080/01490410903297766

Behrenfeld, M. J., Prasil, O., Kolber, Z. S., Babin, M., and Falkowski, P. G. (1998). Compensatory changes in photosystem II electron turnover rates protect photosynthesis from photoinhibition. *Photosynth. Res.* 58, 259–268. doi: 10.1023/A:1006138630573

Chelton, D. B., Gaube, P., Schlax, M. G., Early, J. J., and Samelson, R. M. (2011). The influence of nonlinear mesoscale eddies on near-surface oceanic chlorophyll. *Science* 334 (6054), 328–332. doi: 10.1126/science.1208897

Clayton, S., Nagai, T., and Follows, M. J. (2014). Fine scale phytoplankton community structure across the kuroshio front. *J. Plankton. Res.* 36, 1017–1030. doi: 10.1093/plankt/fbu020

Cullen, J. J. (2015). Subsurface chlorophyll maximum layers: Enduring enigma or mystery solved? *Annu. Rev. Mar. Sci.* 7, 207–239. doi: 10.1146/annurev-marine-010213-135111

Demidov, A. B., Sheberstov, S. V., Gagarin, V. I., and Khlebopashev, P. V. (2017). Seasonal variation of the satellite-derived phytoplankton primary production in the kara Sea. *Oceanology* 57, 91–104. doi: 10.1134/S0001437017010027

Du, C., Liu, Z., Dai, M., Kao, S., Cao, Z., Zhang, Y., et al. (2013). Impact of the kuroshio intrusion on the nutrient inventory in the upper northern south China Sea: insights from an isopycnal mixing model. *Biogeosciences* 10, 6419–6432. doi: 10.5194/bg-10-6419-2013

Ebuchi, N., and Hanawa, K. (2001). Trajectory of mesoscale eddies in the kuroshio recirculation region. *J. Oceanogr.* 57, 471–480. doi: 10.1023/A:1021293822277

Falkowski, P. G., Barber, R. T., and Smetacek, V. (1998). Biogeochemical controls and feedbacks on ocean primary production. *Science* 281 (5374), 200–207. doi: 10.1126/science.281.5374.200

Falkowski, P. G., Ziemmann, D., Kolber, Z., and Bienfang, P. K. (1991). Role of eddy pumping in enhancing primary production in the ocean. *Nature* 352, 55–58. doi: 10.1038/352055a0

Fasham, M. J. R., Ducklow, H. W., and McKelvie, S. M. (1990). A nitrogen-based model of plankton dynamics in the oceanic mixed layer. *J. Mar. Res.* 48, 591–639. doi: 10.1357/002224090784984678

Fiechter, J., Moore, A. M., Edwards, C. A., Bruland, K. W., Lorenzo, E. D., Lewis, C. V. W., et al. (2009). Modeling iron limitation of primary production in the coastal gulf of Alaska. *Deep-Sea Res. II* 56, 2503–2519. doi: 10.1016/j.dsr2.2009.02.010

Garcia, H. E., Locarnini, R. A., Boyer, T. P., and Antonov, J. I. (2006). "World ocean atlas 2005, volume 4: Nutrients (phosphate, nitrate, and silicate)," in *NOAA Atlas NESDIS*, vol. 64 . Ed. S. Levitus (Washington, D.C.: U.S. Government Printing Office), 396 pp.

Gaube, P., Chelton, D. B., Strutton, P. G., and Behrenfeld, M. J. (2013). Satellite observations of chlorophyll, phytoplankton biomass, and ekman pumping in nonlinear mesoscale eddies. *J. Geophys. Res. Oceans* 118, 6349–6370. doi: 10.1002/2013JC009027

Gruber, N., Frenzel, H., Doney, S. C., Marchesiello, P., McWilliams, J. C., Moisan, J. R., et al. (2006). Eddy-resolving simulation of plankton ecosystem dynamics in the California current system. *Deep-Sea Res.* 539, 1483–1516. doi: 10.1016/j.dsr.2006.06.005

Hsu, P.-C., Ho, C.-Y., Lee, H.-J., Lu, C.-Y., and Ho, C.-R. (2020). Temporal variation and spatial structure of the kuroshio-induced submesoscale island vortices observed from GCOM-c and himawari-8 data. *Remote Sens.* 12, 883. doi: 10.3390/rs12050883

Isobe, A., and Imawaki, S. (2002). Annual variation of the kuroshio transport in a two-layer numerical model with a ridge. *J. Phys. Oceanogr.* 32, 994–1009. doi: 10.1175/1520-0485(2002)032<0994:AVOTKT>2.0.CO;2

Kamidaira, Y., Kawamura, H., Kobayashi, T., and Uchiyama, Y. (2019). Development of regional downscaling capability in STEAMER ocean prediction system based on multi-nested ROMS model. *J. Nucl. Sci. Tech.* 56 (8), 752–763. doi: 10.1080/00223131.2019.1613269

Kamidaira, Y., Uchiyama, Y., Kawamura, H., Kobayashi, T., and Furuno, A. (2018). Submesoscale mixing on initial dilution of radionuclides released from the fukushima daiichi nuclear power plant. *J. Geophys. Res. Oceans* 123, 2808–2828. doi: 10.1002/2017JC013359

Kamidaira, Y., Uchiyama, Y., Kawamura, H., Kobayashi, T., and Otosaka, S. (2021). A modeling study on the oceanic dispersion and sedimentation of radionuclides off the coast of fukushima. *J. Environ. Radioact.* 106724, 238–239. doi: 10.1016/j.jenvrad.2021.106724

Kamidaira, Y., Uchiyama, Y., and Mitarai, S. (2017). Eddy-induced transport of the kuroshio warm water around the Ryukyu islands in the East China Sea. *Cont. Shelf Res.* 143, 206–218. doi: 10.1016/j.csr.2016.07.004

Kaneko, H., Yasuda, I., Komatsu, K., and Itoh, S. (2013). Observations of vertical turbulent nitrate flux across the kuroshio. *Geophys. Res. Lett.* 40, 3123–3127. doi: 10.1029/2012gl052419

Kawai, H. (1972). "Hydrography of the kuroshio extension," in *Kuroshio–its physical aspects* (University of Tokyo Press) Tokyo, Japan, 235–354.

Kimura, S., Kasai, A., Nakata, H., Sugimoto, T., Simpson, J. H., and Cheok, J. V. S. (1997). Biological productivity of meso-scale eddies caused by frontal disturbances in the kuroshio. *ICES J. Mar. Sci.* 54, 179–192. doi: 10.1006/jmsc.1996.0209

Klein, P., Hua, B.-L., Lapeyre, G., Capet, X., Le Gentil, S., and Sasaki, H. (2008). Upper ocean turbulence from high-resolution 3D simulations. *J. Phys. Oceanogr.* 38, 1748–1763. doi: 10.1175/2007JPO3773.1

Kodama, T., Shimizu, Y., Ichikawa, T., Hiroe, Y., Kusaka, A., Morita, H., et al. (2014). Seasonal and spatial contrast in the surface layer nutrient content around the kuroshio along 138°E, observed between 2002 and 2013. *J. Oceanogr.* 70, 489–503. doi: 10.1007/s10872-014-0245-5

Koné, V., Machu, E., Penven, P., Andersen, V., Garçon, V., Fréon, P., et al. (2005). Modeling the primary and secondary productions of the southern benguela upwelling system: A comparative study through two biogeochemical models. *Global Biogeochem. Cycles* 19, GB4021. doi: 10.1029/2004GB002427

Kouketsu, S., Kaneko, H., Okunishi, T., Sasaoka, K., Itoh, S., Inoue, R., et al. (2014). Mesoscale eddy effects on temporal variability of surface chlorophyll a in the kuroshio extension. *J. Oceanogr.* 72, 439–451. doi: 10.1007/s10872-015-0286-4

Kurosawa, K., Uchiyama, Y., and Kosako, T. (2020). Development of a numerical marine weather routing system for coastal and marginal seas using

regional oceanic and atmospheric simulations. *Ocean Eng.* 195, 106706. doi: 10.1016/j.oceaneng.2019.106706

Large, W. G., McWilliams, J. C., and Doney, S. C. (1994). Oceanic vertical mixing: A review and model with a nonlocal boundary layer parameterization. *Rev. Geophys.* 32, 363–403. doi: 10.1029/94RG01872

Lazzari, P., Solidoro, C., Ibello, V., Salon, S., Teruzzi, A., Béranger, K., et al. (2012). Seasonal and inter-annual variability of plankton chlorophyll and primary production in the Mediterranean Sea: a modelling approach. *Biogeosciences* 9, 217–233. doi: 10.5194/bg-9-217-2012

Lee, E. A., and Kim, S. Y. (2018). Regional variability and turbulent characteristics of the satellite-sensed submesoscale surface chlorophyll concentrations. *J. Geophys. Res. Oceans* 123, 4250–4279. doi: 10.1029/2017JC013732

Lemarié, F., Kurian, J., Shchepetkin, A. F., Molemaker, M. J., Colas, F., and McWilliams, J. C. (2012). Are there inescapable issues prohibiting the use of terrain-following coordinates in climate models? *Ocean Modell.* 42, 57–79. doi: 10.1016/j.ocemod.2011.11.007

Liu, X., and Levine, N. M. (2015). Enhancement of phytoplankton chlorophyll by submesoscale frontal dynamics in the north pacific subtropical gyre. *Geophys. Res. Lett.* 43, 1651–1659. doi: 10.1002/2015GL066996

Lomas, M. W., Moran, S. B., Casey, J. R., Bell, D. W., Tiahlo, M., Whitefield, J., et al. (2012). Spatial and seasonal variability of primary production on the Eastern Bering Sea shelf. *Deep-Sea Res. II* 65-70, 126–140. doi: 10.1016/j.dsr2.2012.02.010

Marchesiello, P., McWilliams, J. C., and Shchepetkin, A. (2003). Equilibrium structure and dynamics of the California current system. *J. Phys. Oceanogr.* 33, 753–783. doi: 10.1175/1520-0485(2003)33<753:ESADOT>2.0.CO;2

Mason, E., Molemaker, J., Shchepetkin, A. F., Colas, F., McWilliams, J. C., and Sangrà, P. (2010). Procedures for offline grid nesting in regional ocean models. *Ocean Modell.* 35, 1–15. doi: 10.1016/j.ocemod.2010.05.007

Masunaga, E., Uchiyama, Y., Suzue, Y., and Yamazaki, H. (2018). Dynamics of internal tides over a shallow ridge investigated with a high-resolution downscaling regional ocean model. *Geophys. Res. Lett.* 45, 8, 3550–3558. doi: 10.1002/2017GL076916

Masunaga, E., Uchiyama, Y., and Yamazaki, H. (2019). Strong internal tides generated by the interaction of the kuroshio current and tides over a shallow ridge. *J. Phys. Oceanogr.* 49, 11, 2917–2934. doi: 10.1175/JPO-D-18-0238.1

Masunaga, E., Uchiyama, Y., Zhang, X., Kimura, W., and Kosako, T. (2022). Modulation of submesoscale eddies and associated Lagrangian transport due to tides and shallow ridge along the kuroshio. *Deep-Sea Res. Part I* 186, 103828. doi: 10.1016/j.dsr.2022.103828

Matsushita, K., Uchiyama, Y., Takaura, N., and Kosako, T. (2022). Fate of river-derived microplastics from the south China Sea: Sources to surrounding seas, shores, and abysses. *Environ. Pollut.* 308. doi: 10.1016/j.envpol.2022.119631

Miyazawa, Y., Zhang, R., Guo, X., Tamura, H., Ambe, D., Lee, J., et al. (2009). Water mass variability in the Western north pacific detected in 15-year eddy resolving ocean reanalysis. *J. Oceanogr.* 65, 737–756. doi: 10.1007/s10872-009-0063-3

Moore, C. W., Mills, M. M., Arrigo, K. R., Berman-Frank, I., Bopp, L., Boyd, P. W., et al. (2013). Processes and patterns of oceanic nutrient limitation. *Nat. Geosci.* 6, 701–710. doi: 10.1038/NGEO1765

Nagai, T., Clayton, S., and Uchiyama, Y. (2019). "Multiscale routes to supply nutrients through the kuroshio nutrient stream," in *Kuroshio current: Physical, biogeochemical and ecosystem dynamics, geophysical monograph series.* Eds. T. Nagai, H. Saito, K. Suzuki and M. Takahashi (NY: John Wiley & Sons), ISBN: 1119428343.

Nagai, T., Gruber, N., Frenzel, H., Lachkar, Z., McWilliams, J. C., and Plattner, G. (2015). Dominant role of eddies and filaments in the offshore transport of carbon and nutrients in the California current system. *J. Geophys. Res. Oceans* 120, 5318–5341. doi: 10.1002/2015JC010889

Nagai, T., Hasegawa, D., Tanaka, T., Nakamura, H., Tsutsumi, E., Inoue, R., et al. (2017). First evidence of coherent bands of strong turbulent layers associated with high-wavenumber internal- wave shear in the upstream kuroshio. *Sci. Rep.* 7, 14555. doi: 10.1038/s41598-017-15167-1

Nagai, T., Tandon, A., Yamazaki, H., Doubell, M. J., and Gallager, S. (2012). Direct observations of microscale turbulence and thermohaline structure in the kuroshio front. *J. Geophys. Res.* 117, C08013. doi: 10.1029/2011JC007228

Nakata, H., Kimura, S., Okazaki, Y., and Kasai, A. (2000). Implications of meso-scale eddies caused by frontal disturbances of the kuroshio current for anchovy recruitment. *ICES J. Mar. Sci.* 57, 143–152. doi: 10.1006/jmsc.1999.0565

C. Nellemann, E. Corcoran, C. M. Duarte, L. Valdés, C. De Young, L. Fonseca and G. Grimsditch (Eds.) (2009). *Blue carbon. a rapid response assessment, united nations environment programme, GRID-arendal, birkeland trykkeri AS* (Norway), 78 pp.

Nishibe, Y., Takahashi, K., Shiozaki, T., Kakehi, S., Saito, H., and Furuya, K. (2015). Size-fractionated primary production in the kuroshio extension and adjacent regions in spring. *J. Oceanogr.* 71, 27–40. doi: 10.1007/s10872-014-0258-0

Nishikawa, H., Yasuda, I., Komatsu, K., Sasaki, H., Sasai, Y., Setou, T., et al. (2013). Winter mixed layer depth and spring bloom along the kuroshio front: implications for the Japanese sardine stock. *Mar. Ecol. Prog. Ser.* 487, 217–229. doi: 10.3354/meps10201

Oey, L. Y. (2008). Loop current and deep eddies. *J. Phys. Oceanogr.* 38 (7), 1426–1449. doi: 10.1175/2007JPO3818.1

Oschlies, A. (2001). Model-derived estimates of new production: New results point towards lower values. *Deep Sea Res. Part II: Topical Stud. Oceanography* 48 (10), 2173–2197. doi: 10.1016/S0967-0645(00)00184-3

Park, K., Kang, C., Kim, K., and Park, J. (2014). Role of sea ice on satellite-observed chlorophyll-a concentration variations during spring bloom in the East/Japan sea. *Deep-Sea Res.* 47, 34–44. doi: 10.1016/j.dsr.2013.09.002

Qiu, B. (2002). The kuroshio extension system: its large-scale variability and role in the midlatitude ocean-atmosphere interaction. *J. Oceanogr.* 58, 57–75. doi: 10.1023/A:1015824717293

Roads, J. (2004). Experimental weekly to seasonal U.S. forecasts with the regional spectral model. *Bull. Amer. Meteor. Soc* 85, 1887L1902. doi: 10.1175/BAMS-85-12-1887

Rodriguez, E., Morris, C. S., and Belz, J. E. (2006). A global assessment of the SRTM performance. *Photogramm. Eng. Rem. Sens* 72 (3), 249–260. doi: 10.14358/PERS.72.3.249

Rodriguez, E., Morris, J. E., Belz, J. E., Chapin, E. C., Martin, J. M., Daffer, W., et al. (2005). *An assessment of the SRTM topographic products. technical report* (Pasadena, CA: Jet Propulsion Laboratory).

Sangrà, P. (2015). "Canary islands eddies and coastal upwelling filaments off north-west Africa," in *Oceanographic and biological features in the canary current Large marine ecosystem*, vol. 115 . Eds. L. Valdés and I. Déniz- González (Paris: IOC-UNESCO), 105–114. Available at: http://hdl.handle.net/1834/9181. IOC Technical Series.

Sasai, Y., Richards, K. J., Ishida, A., and Sasaki, H. (2010). Effects of cyclonic mesoscale eddies on the marine ecosystem in the kuroshio extension region using an eddy-resolving coupled physical-biological model. *Ocean Dyn.* 60, 693–704. doi: 10.1007/s10236-010-0264-8

Sasai, Y., Sasaoka, K., Sasaki, H., and Ishida, A. (2007). Seasonal and intra-seasonal variability of chlorophyll-a in the north pacific: model and satellite data. *J. Earth Sim.* 8, 3–11. doi: 10.32131/jes.8.3

Sasaki, H., Klein, P., Qiu, B., and Sasai, Y. (2014). Impact of oceanic-scale interactions on the seasonal modulation of ocean dynamics by the atmosphere. *Nat. Commun.* 5, 5636. doi: 10.1038/ncomms6636

Schimel, D. S., House, J. I., Hibbard, K. A., Bousquet, P., Ciais, P., Peylin, P., et al. (2001). Recent patterns and mechanisms of carbon exchange by terrestrial ecosystems. *Nature* 414, 169–172. doi: 10.1038/35102500

Shchepetkin, A. F., and McWilliams, J. C. (2005). The regional ocean modeling system (ROMS): a split-explicit, free-surface, topography-following-coordinate oceanic model. *Ocean Modell.* 9, 347–404. doi: 10.1016/j.ocemod.2004.08.002

Shchepetkin, A. F., and McWilliams, J. C. (2008). "Computational kernel algorithms for fine-scale, multiprocess, longtime oceanic simulations," in *Handbook of numerical analysis: Computational methods for the ocean and the atmosphere*. Eds. R. Temam and J. Tribbia (Amsterdam: Elsevier), 119–181. doi: 10.1016/S1570-8659(08)01202-0

Sugimoto, S., and Hanawa, K. (2012). Relationship between the path of the kuroshio in the south of Japan and the path of the kuroshio extension in the east. *J. Oceanogr.* 68, 219–225. doi: 10.1007/s10872-011-0089-1

Tada, H., Uchiyama, Y., and Masunaga, E. (2018). Impacts of two super typhoons on the kuroshio and marginal seas on the pacific coast of Japan. *Deep-Sea Res. Part I* 132, 80–93. doi: 10.1016/j.dsr.2017.12.007

Takeda, N., Kashima, M., Odani, S., Uchiyama, Y., Kamidaira, Y., and Mitarai, S. (2021). Identification of coral spawn source areas around sekisei lagoon for recovery and poleward habitat migration by using a particle-tracking model. *Sci. Rep.* 11, 6963. doi: 10.1038/s41598-021-86167-5

Thomas, L. N., and Lee, C. M. (2005). Intensification of ocean fronts by down-front winds. *J. Phys. Oceanogr.* 35, 1086–1102. doi: 10.1175/JPO2737.1

Thomas, L. N., and Taylor, J. R. (2010). Reduction of the usable wind-work on the general circulation by forced symmetric instability. *Geophys. Res. Lett.* 37, L18606. doi: 10.1029/2010GL044680

Uchiyama, Y., Idica, E., McWilliams, J. C., and Stolzenbach, K. D. (2014). Wastewater effluent dispersal in southern California bays. *Cont. Shelf Res.* 76, 36–52. doi: 10.1016/j.csr.2014.01.002

Uchiyama, Y., Kanki, R., Takano, A., Yamazaki, H., and Miyazawa, Y. (2018b). Mesoscale reproducibility in regional ocean modeling with a 3-d stratification estimate based on aviso-argo data. *Atmosphere-Ocean* 56, 4, 212–4, 229. doi: 10.1080/07055900.2017.1399858

Uchiyama, Y., Odani, S., Kashima, M., Kamidaira, Y., and Mitarai, S. (2018a). Influences of the kuroshio on interisland remote connectivity of corals across the nansei archipelago in the East China Sea. *J. Geophys. Res. Oceans* 123, 9245–9265. doi: 10.1029/2018JC014017

Uchiyama, Y., Suzue, Y., and Yamazaki, H. (2017). Eddy-driven nutrient transport and associated upper-ocean primary production along the kuroshio. *J. Geophys. Res. Oceans* 122, 5046–5062. doi: 10.1002/2017JC012847

Uchiyama, Y., Tokunaga, N., Aduma, K., Kamidaira, Y., Tsumune, D., Iwasaki, T., et al. (2022). A storm-induced flood and associated nearshore dispersal of the river-derived suspended $^{137}$Cs. *Sci. Total Environ.* 816, 151573. doi: 10.1016/j.scitotenv.2021.151573

Uchiyama, Y., Zhang, X., Suzue, Y., Kosako, T., Miyazawa, Y., and Nakayama, A. (2018c). Residual effects of treated effluent diversion on a seaweed farm in a tidal strait using a multi-nested high-resolution 3-d circulation-dispersal model. *Mar. Pollut. Bull.* 130, 40–54. doi: 10.1016/j.marpolbul.2018.03.007

Uitz, J., Claustre, H., Gentili, B., and Stramski, D. (2010). Phytoplankton class-specific primary production in the world's oceans: Seasonal and interannual variability from satellite observations. *Global Biogeochem. Cycles* 24, GB3016. doi: 10.1029/2009GB003680

Woodruff, S. D., Slutz, R. J., Jenne, R. L., and Steurer, P. M. (1987). A comprehensive ocean- atmosphere data set. *Bull. Am. Meteorolog. Soc.* 68, 1239–1250. doi: 10.1175/1520-0477(1987)068<1239:ACOADS>2.0.CO;2

Xu, L., Xie, S., Jing, Z., Wu, L., Liu, Q., Li, P., et al. (2016). Observing subsurface changes of two anticyclonic eddies passing over the izu-ogasawara ridge. *Geophys. Res. Lett.* 44, 1857–1865. doi: 10.1002/2016GL072163

Yamada, K., Ishizaka, J., Yoo, S., Kim, H., and Chiba, S. (2004). Seasonal and interannual variability of sea surface chlorophyll *a* concentration in the Japan/East Sea (JES). *Prog. Oceanogr.* 61, 193–211. doi: 10.1016/j.pocean.2004.06.001

Yoo, S., and Kim, H. (2003). Suppression and enhancement of the spring bloom in the southwestern East Sea/Japan Sea. *Deep-Sea Res. II* 51, 1093–1111. doi: 10.1016/j.dsr2.2003.10.008

Zhang, X., Uchiyama, Y., and Nakayama, A. (2019). On relaxation of the influences of treated sewage effluent on an adjacent seaweed farm in a tidal strait. *Mar. Pollut. Bull.* 144, 265–274. doi: 10.1016/j.marpolbul.2019.04.050